SERS Study of N-heterocyclic Carbenes Absorbed on a Silver Electrode

by

Mengxin Ge
B.Sc., St. Francis Xavier University, 2017,

A Thesis Submitted in Partial Fulfillment
of the Requirements for the Degree of

MASTER OF SCIENCE

in the Department of Chemistry

Supervisory Committee

SERS Study of N-heterocyclic Carbenes Absorbed on a Silver Electrode

by

Mengxin Ge
B.Sc., St. Francis Xavier University, 2017

Supervisory Committee

Dr. Alexandre G. Brolo, Department of Chemistry
Supervisor

Dr. Dennis Hore, Department of Chemistry
Departmental Member

Abstract

Supervisory Committee
Dr. Alexandre G. Brolo, Department of Chemistry
Supervisor
Dr. Dennis Hore, Department of Chemistry
Departmental Member

SERS (surface-enhanced Raman spectroscopy) has the potential to be used in a variety of commercial and basic applications, which often rely on molecules that are bound to a nanostructured metal surface. Thiols are usually used as the intermediate to modify the substrate surface for SERS. In recent years, N-heterocyclic carbene (NHC) has been introduced as an alternative approach for metal surface modification. Nanostructured gold surfaces suitable for SERS had been modified by NHC species. Those studies showed the promising of the NHC modification route for the fabrication of a robust platform for SERS.

The objective of this work is to explore the SERS characteristics of NHC species on silver surfaces. The interactions between two different NHC molecules and a nanostructured silver surface, instead of a gold surface, were studied for the first time. The experiments were realized in electrochemical conditions, using a three-electrodes system, to fully test the stability of the NHC-modified surfaces. The SERS spectra were compared to theoretical calculations and normal Raman in order to identify the vibrational characteristics of the NHC molecules. The effects of different NHC molecule substituents on the electrochemical stability of the surface were also discussed. The results showed that NHC molecules can be decomposed on the silver surface easily under electrochemical conditions. This contrast with the observations in gold, where the NHC monolayers showed a high level of stability.

This work also discusses potential side products which may be derived from the decomposition of the NHC molecules. Raman spectra of potential side products were collected and compared to the NHC SERS collected under electrochemical control at different potentials.

This study provides insights into the influence of the substituents at the NHC on their stability under the electrochemical condition, which should guide the development of future applications.

Table of Contents

List of Tables

List of Figures

List of Schemes

Acknowledgments

"Life is a long journey, with problems to solve, lessons to solve, lessons to learn, but most of all, experiences to enjoy."

The completion of this Master's thesis has been an adventurous and incredible journey for me. Especially when the world has changed a lot during this journey because of an evil called Covid.

Throughout the writing of this dissertation, I have received a great deal of support and assistance. Firstly and most importantly, I would like to give my heartfelt gratitude to my supervisor, Dr. A. G. Brolo, for his extended patience and encouragement these past years. Without his help, this dissertation would not have been completed. He always applies an appropriate amount of pressure when I felt lost during the journey with enough support and useful guidance.

I would like to thank the Brolo-group student, especially Yu-De Lin who helped me with all the Gaussian theoretical calculation parts. Their help is always inspired and encouraged me a lot.

I am especially thankful to Dr. Stanislav Konorov and Alex Wlasenko for their help with all the equipment assistance with their professional knowledge and sufficient patience. Dr. Stanislav Konorov helped me a lot with the design of the microscope stage. Without him, the experiment would not have been done.

I owe many thanks to my family for the completion of this task. I would like to thank my parents, Wenbo Gai, and Xuejie Guan, and my grandparents, Yunjie Gai, and Zhengzhen Rui, who always provide me unconditional support, no matter how long my journey took. They always are my strong support, every time I feel difficult. In addition

to saving me from the dead-end of this journey. I love them 3000, like how much they love me.

Last, I appreciate all the experience in this journey, no matter good or bad, that makes me stronger.

The journey continues…
Mengxin Ge

Chapter 1 - Introduction

1.1 Organization of the Thesis

This thesis is divided into four chapters including this first introduction chapter.

In chapter one, brief background information required for the readers to understand this research is presented. The first section gives a general overview of Raman Scattering (Section 1.2), followed by the introduction of the surface-enhanced Raman scattering (SERS) effect, which is the fundamental technique used in the experiments (Section 1.3). In Section 1.4, N-Heterocyclic Carbenes (NHCs) are introduced to provide the basic idea of the motivation for this study.

Chapter two covers the details of experimental setups for both Raman and SERS (including electrochemical SERS) measurements. The process of preparing the SERS-active silver electrode surface is also introduced in this chapter, as well as an overview of the theoretical calculation used in this study.

In chapter three, all the experimental results are discussed, including the Raman, SERS measurements, and theoretical calculations for the two types of NHCs studied in this research. A discussion about the experimental findings is also presented.

Chapter four gives a brief conclusion of the main findings in this thesis and a perspective for future studies. References for all chapters are at the end of the thesis, right after chapter four.

1.2 Raman Scattering

1.2.1 History

When light interacts with matter, it may be absorbed, scattered, or simply pass through the substance. It can also induce photochemical processes. If the energy of the incident photon corresponds to the gap between a ground state and an excited state in the material, the photon might be absorbed, leading to an excited state. On the other hand, the photon could just scatter through interactions with the molecules. For example (Figure 1.1), the sky is blue because of the Rayleigh scattering; Tyndall scattering makes a light beam visible in a fog. Both the Rayleigh and Tyndall scattering are elastic scattering, where the energy of the incident light is the same as the scattered light. In some other cases, however, there is a change of energy after the light is scattered by the molecules. Those are inelastic phenomena in which the energy (or wavelength) of the incident light is not the same as the scattered light. The Raman process is an example of inelastic scattering. Experimentally, the scattered photons are detected at a certain angle relative to the incident light, which is typically a laser source. Raman scattering can be used to identify molecules and it is one of the most widely used scattering techniques in analytical and physical chemistry.[1]

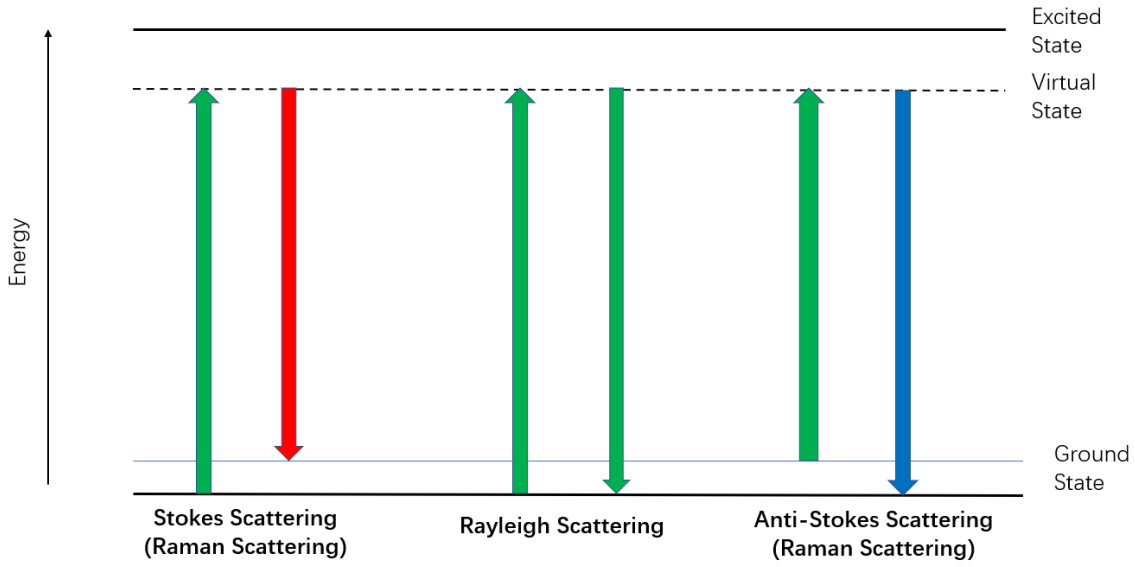

Figure 1.1 Schematic diagram of Raman and Rayleigh scattering. Gain or loss of energy (indicated by the blue and red arrow) resulting in Raman scattering (Stokes and Anti-Stokes scattering). Rayleigh scattering occurs when the incident light energy E_0 is equal to the scattered light energy E.

First observed in 1928 by Raman and Krishnan,[2] Raman scattering is basically the inelastic scattering of photons from molecules. Relying on the Raman scattering, Raman spectroscopy plays an important role in physics,[3] biology,[4, 5], and materials science.[6] Raman spectroscopy has been widely used in chemistry to determine vibrational spectra which provide a structural fingerprint for molecule identification.[7]

Since water and glass have much weaker signals in Raman spectroscopy than that in other spectroscopies, also, compared with water and glass, the Raman signal of most analytes is much stronger, and the interference with the Raman spectrum can be almost ignored. Hence, Raman Spectroscopy is superior to other vibrational spectroscopies especially when testing liquid samples.[8, 9]

1.2.2 Basic Description of Raman Scattering

The Jablonski diagram[10] is widely used to describe the energy transitions between electronic states of a molecule in molecular spectroscopy.[11-13] Figure 1.1 is an example of a Jablonski diagram that demonstrates the possible energy transitions between an electronic ground state (S_0) and a singlet state (S_1). Each electronic state represents the corresponding energy level of the molecule. When electrons occupy the ground electronic state, all electrons are paired in the particular example of Figure 1.1. According to the Pauli exclusion principle, the electrons occupy the lowest energy at the ground electronic state.[14]

As a central principle in quantum mechanics,[15] molecular vibrational energy is confined to certain states without steps between two levels.

The relation between the energy of a photon and the wavelength of an electromagnetic wave can be described as equation (1.1) where h is Planck's constant, c is the speed of light and λ is the wavelength.

$$E = hc/\lambda \qquad (1.1)$$

The energy difference (ΔE) between vibrational levels v_0 and v_1 at the electronic ground state depends on the natural frequency of the vibration. The energy difference (ΔE) between vibrational states, then, can be probed using photons with the appropriated energy. Since the vibrational signature is unique for a given species, molecular spectroscopy is used to identify different molecules.

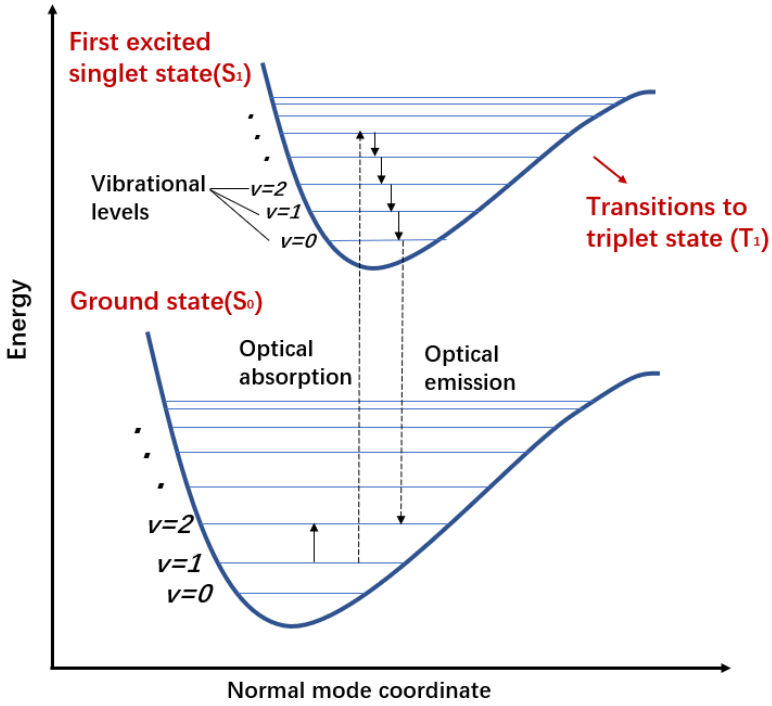

Figure 1.2 Schematic diagram of electronic states (bold lines) and vibrational energy levels with a Jablonski diagram. The arrows indicate possible transitions that can occur between the ground state **(S_0)** and the first excited singlet state **(S_1).**

Luminescence can be defined as the process involving an electron that is excited to a higher electronic state (absorption) that subsequently relaxes to a lower level of energy while emitting a photon (emission). Fluorescence is the most common type of luminescence. The Jablonski diagram in Fig. 1.2 describes how fluorescence occurs as a two steps spontaneous emission process. An electron in a molecule undergoes an adsorption process when excited by the incident photon with energy E_0 from a sub-level (v=0, 1, 2, etc.) of the electron ground state S_0 into a sub-level of the excited state S_1. The electron then relaxes down to the lowest energy level of S_1. From that, spontaneous emission may occur with the election relaxing down to the electronic ground state S_0, followed by the emission of a photon. The emitted photon has an energy E which is lower than the incident photon energy E_0.

Fluorescence involves an intermediate step (Fig. 1.2), while there is another important family of processes that requires instantaneous adsorption of an incident photon and emission of another photon. Those processes are called scattering processes and there are two main groups of scattering processes, elastic scattering, and inelastic scattering. The inelastic scattering of photons by molecules is known as Raman scattering, indicated in Fig. 1.1, and it can be classified into anti-Stokes and Stokes scattering, depending on if the scattered energy E is higher or lower than the incident energy, respectively.

The difference between Raman scattering (Fig. 1.1) and fluorescence (Fig. 1.2) is that scattering does not involve an intermediate step. This means the electronic excitation followed by emission with a limited lifetime does not exist in the scattering process. Therefore, the scattering can happen without direct absorption (the direct excitation of the electron to a real excited state). To help explain and understand this better, the scattering process can be broken down into two steps, as indicated in Figure 1.3. In the absorption step, the electron should be excited to a higher electronic energy level. However, in a Raman process, this energy level is unobservable and may not really exist. The intermediate step is then represented as a virtual state. As illustrated in Fig. 1.3 (a), fluorescence occurs with an intermediate step and the electron is excited to a real higher-energy level state S_1. Figs. 1.3 (b), (c), (d), shows that when scattering occurs, the electron is excited to an intermediate virtual state followed by emission. When the incident energy is equivalent to the scattered energy, which means there is no transfer energy between the molecule and the photon, the process is referred to as Rayleigh scattering (Fig. 1.3 (b)). Otherwise, it will be Raman scattering (Fig. 1.3 (c), (d))

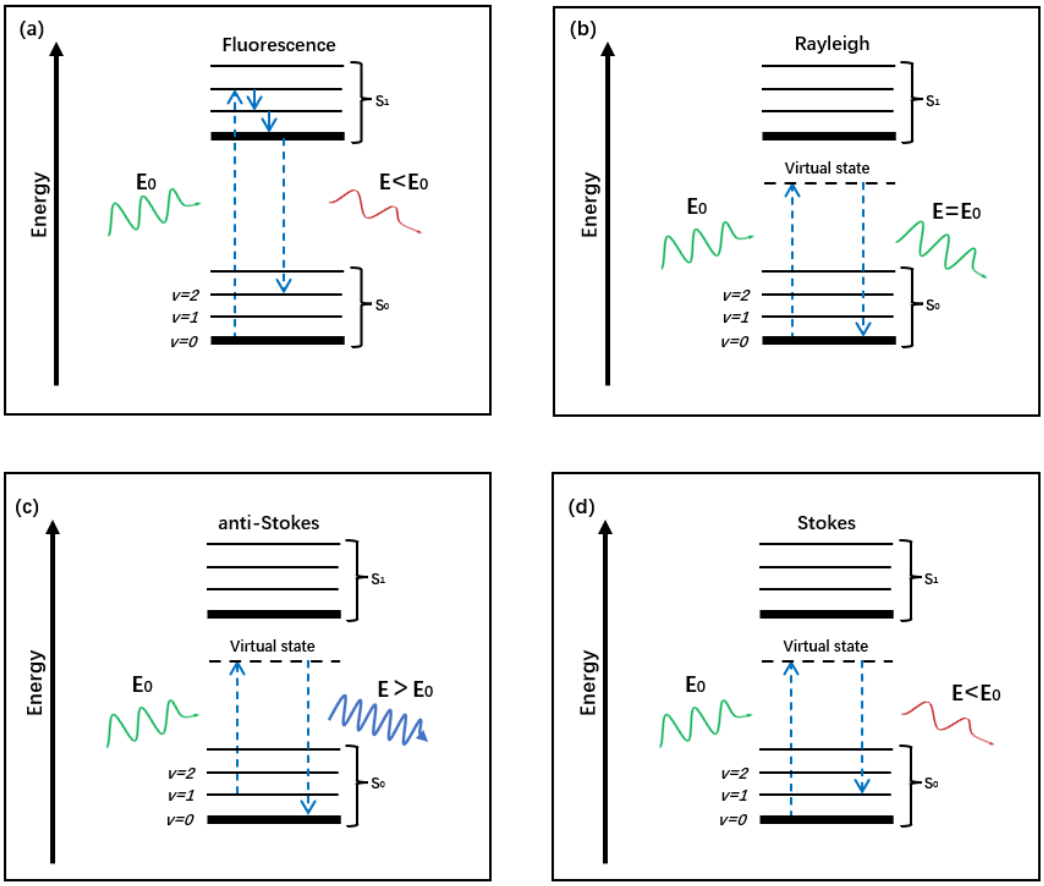

Figure 1.3 Simplified Jablonski diagrams illustrate schematically the fluorescence process in a molecule (a), Rayleigh scattering (b), and Raman scattering (c), (d). Different from the fluorescence process, the incident photon energy E_0 does not need to be excited to a real electronic state of the molecule for the scattering process. With the intermediate virtual state in (b), (c), and (d), the scattering can then be considered a two-steps processes. First, the adsorption of a photon through a transition to an intermediate virtual state followed by an emission back to the sub-level of the ground electronic state S_0.

The three types of scattering represented in the Jablonski diagrams in Fig. 1.3 are further illustrated in Figure 1.4. Raman scattering with the incident light energy E_0 higher than the scattered light energy E is called Stokes scattering. On the other hand, when the incident light energy E_0 is lower than the scattered light energy E, the process is called anti-

Stokes scattering. When the incident light energy E_0 is equivalent to the scattered light energy E, it is called Rayleigh scattering.

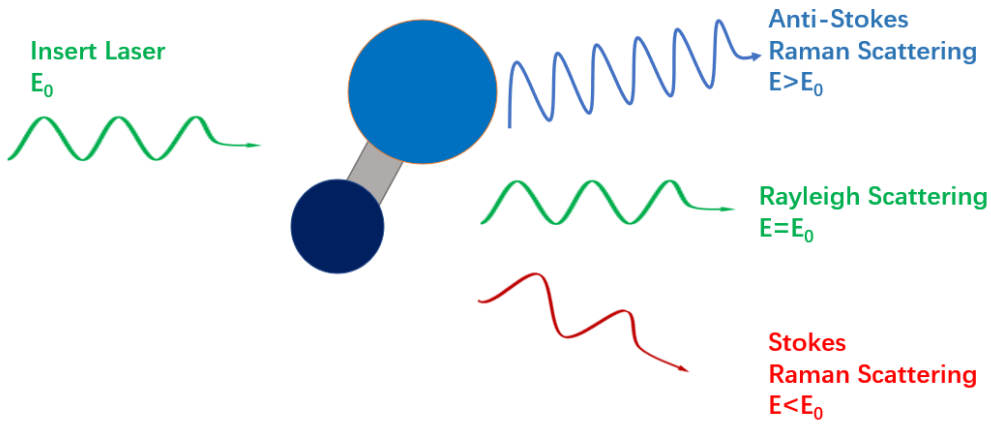

Figure 1.4 Scattering of light when interacting with the molecule. The incident photon hit the molecule with energy E_0. When the scattered light energy E is higher than E_0, it is called Stokes Raman scattering (red). On the contrary, when the incident light energy E_0 is lower than the scattered light energy E, it is called Anti-Stokes scattering (blue). When the incident light energy E_0 is equivalent to the scattered light energy E, it is called Rayleigh scattering (green).

Classically, as shown in Figure 1.5, Raman scattering can be explained by the interaction between an incident electric field and a molecule through polarizability and producing a radiation dipole moment:[16, 17]

$$\mathbf{P} = \alpha \mathbf{E} \qquad (1.2)$$

where the induced polarization (P) is related to the polarizability (α) and the incident field (E).

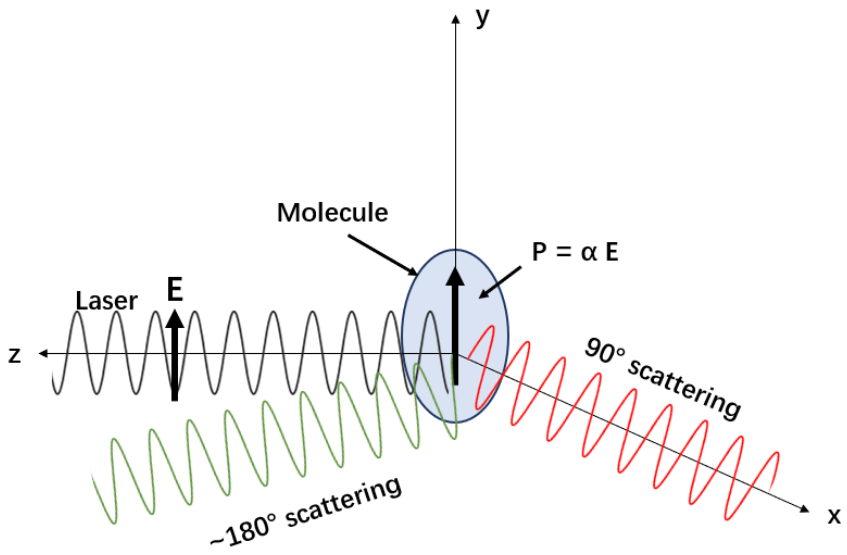

Figure 1.5 Induced Polarization (P) caused by an incident electric field (E) in an electron cloud of a molecule.

The definition of the incident electric field (E) at a given time t can be described by the scattering light from the start of the molecule, as in equation 1.3:

$$E = E_0 \cos(2\pi\nu_0 t) \qquad (1.3)$$

where ν_0 is the frequency of the excitation laser.

The vibrational motion of a molecule can be described as a linear combination of its normal modes. A nonlinear molecule consisting of N atoms has 3N-6 normal modes, Q_i. Q can be described in the equation (1.4), where ν_i is the harmonic frequency of the *i*th mode.

$$Q_i = Q_i^0 cos 2\pi\nu_i t \qquad (1.4)$$

The changing polarizability caused by the small displacements can be described in a Taylor series:

$$\alpha = \alpha_0 + \left(\frac{\delta\alpha}{\delta Q_i}\right)_0 Q_i + \cdots \quad (1.5)$$

Combining equation (1.2) with (1.3) and (1.5), we can obtain:

$$P_i = \alpha_0 E_0 \cos(2\pi\nu_0 t) + E_0 Q_i^0 \left(\frac{\delta\alpha}{\delta Q_i}\right)_0 \cos(2\pi\nu_0 t)\cos(2\pi\nu_i t) \quad (1.6)$$

Employing the trigonometric identity $\cos(x)\cos(y) = \frac{1}{2}[\cos(x+y) + \cos(x-y)]$ into the equation (2.5), we can obtain:

$$P_i = \alpha_0 E_0 \cos(2\pi\nu_0 t) + \frac{1}{2} E_0 Q_i^0 \left(\frac{\delta\alpha}{\delta Q_i}\right)_0 \cos[2\pi(\nu_0 + \nu_i)t] + \frac{1}{2} E_0 Q_i^0 \left(\frac{\delta\alpha}{\delta Q_i}\right)_0 \cos[2\pi(\nu_0 - \nu_i)t] \quad (1.7)$$

This equation is very important and useful not only because it describes most of the characteristics of the scatter light, but also because it illustrates the result of the selection rules of Raman scattering: A change of the polarization of a molecule must happen during the vibration in order for a vibrational mode to be Raman active.[18] Mathematically,

$$\left(\frac{\delta\alpha}{\delta Q_i}\right)_0 \neq 0 \quad (1.8)$$

This means that the first term in equation (1.7) correspond to Rayleigh scattering while the second and third term represents the anti-Stokes and the Stokes scattering, respectively.

1.2.3 Resonance Raman Scattering

As described in Section 1.2.2, Raman scattering happens when the molecule is excited to an intermediate energy state called a 'virtual state' (Figure 1.1). However, an important aspect of Raman cannot be explained by the classical Raman theory introduced in Section 1.2.2. which is the resonance Raman scattering. When the molecule is excited to a higher real electronic state instead of the virtual state, a significant enhancement of the Raman signal is observed. This phenomenon is called resonance Raman scattering. It occurs when the energy of the incident photon meets the requirement for the electronic transition. Resonance Raman scattering is significantly important since it is more sensitive and can enhance Raman scattering intensities by ~10^2-10^6 times compare with ordinary Raman scattering[19].

1.3 Surface-Enhanced Raman Scattering (SERS)

1.3.1 History

In 1974, Fleischmann *et al.* first observed enhanced Raman scattering signals from pyridine adsorbed on a rough silver surface in an electrochemical cell.[20] However, they did not realize that was a new Raman scattering phenomenon and simply assigned the

enhancement to an increase in surface area. In 1977, Jeanmaire and Van Duyne,[21] Albrecht and Creighton[22] independently repeated Fleischmann *et al.*'s experiment and observed that the Raman signal from the pyridine molecules had been amplified by ~10^6 times. They suggested that the mechanism for the enhanced Raman effect should be related to the nature of the substrate rather than simply surface area and that the surface structure plays a very important role in this effect. This phenomenon is called surface-enhanced Raman scattering (SERS).

The mainstream mechanisms of SERS can be divided into two categories: electromagnetic (EM) effect and charge-transfer (CT) effect/ chemistry effect (CE). The electromagnetic (EM) effect is widely considered the main contribution to the enhancement factor and it arises from the coupling of the incident and Raman electromagnetic fields with the metallic nanostructure.

In the following years, the surface-enhanced Raman scattering (SERS) effect has been observed on various metal surfaces with different molecules. The discovery of SERS is not only a hope for electrochemists but also attracts the attention of the fields of analytical chemistry, physics, optics, catalysis, colloid science, engineering, biology, etc. In 1985, Moskovits[23] provided a great summary of SERS activity in a review up to that time. More modern perspective aspects of SERS are also summarized by Langer[24] in 2019

1.3.2 Basic Principles

Surface-enhanced Raman scattering (SERS) is a surface-sensitive technique that amplifies Raman signals by several orders of magnitude on a nanostructured metallic

surface. The major point for the application of SERS is the 'surface' in which the molecule must be on or close enough to be detected. The main difference between Raman and SERS is the requirement of metallic nanostructure as the substrate for the analyte to absorb (Figure 1.6).

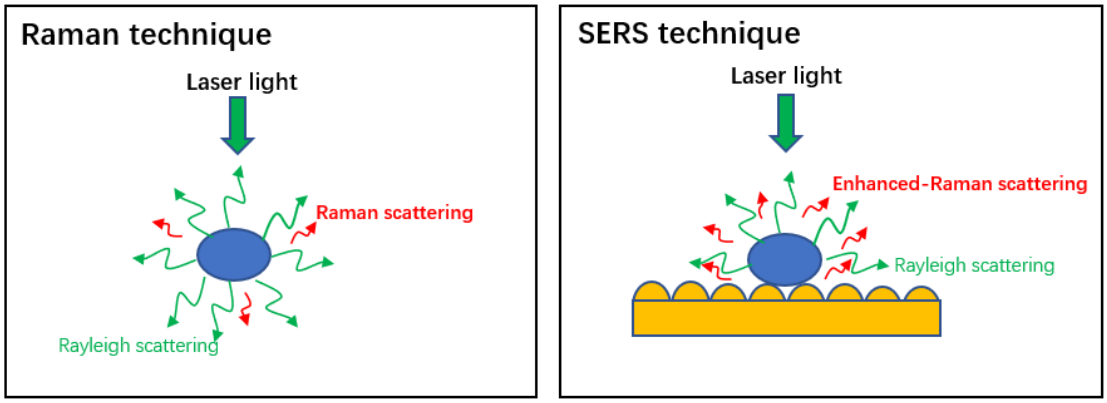

Figure 1.6 The basic principles of Raman and SERS techniques. With the metallic nanostructure as the substrate, it can enhance ~10^2-10^6 times Raman scattering intensity compare with ordinary Raman scattering.

1.3.3 Electromagnetic (EM) and Charge-transfer (CT) Enhancement Factors

As described in Section 1.3.1, two main proposed theories, electromagnetic (EM) and charge transfer (CT), contribute to the enhancement of the SERS effect. The electromagnetic enhancement model is a physical model which is expressed as an enhancement of the electric field produced at the metal surface that amplifies the Raman signal from the adsorbed analyte. Kerker[25-29] *et al*. proposed that a small, isolated,

illuminated metal particle is surrounded by electromagnetic fields. When the incident electromagnetic field strikes the metal surface, localized surface plasmons are excited. The plasmon oscillations must be perpendicular to the surface to allow efficient scattering. Otherwise, if the plasmon oscillations are parallel to the metal surface, the scattering does not occur.[19]

A simplified electromagnetic enhancement model for SERS is illustrated in Figure 1.7. Both particles and molecules are excited by the incident field. Because the distance between a molecule is close enough to a particle, coupling between the two dipole fields can be excited. The easier way to understand this system is to consider it as a two-step process.

The following discussion about the SERS enhancement factor is based on the discussion in Ref. 30. For process 1 (green in Figure 1.7), the particle's localized surface plasmons are excited by the incident electromagnetic field, E_0. The induced oscillating dipoles can be given by $p = \alpha_p E$, where α_p is the particle polarizability tensor. The induced polarization generates large local fields $E_{0,\,loc}$ on the particle and it enhances the incident field by $(E_0+E_{0,\,loc})$. The Raman scattering is excited by the total field. Because the Raman intensity is proportional to the square field, it gives $I\sim (E_0+E_{0,\,loc})^2$. For process 2 (blue in Figure 1.7), the emitted Raman field from the molecule E_{mol} can also be enhanced by the metal particles. The Raman intensity is then $I\sim (E_{mol}+E_{mol,\,loc})^2$. As a result, the Raman signal is enhanced as E^2 at each process, for a total enhancement of E^4.

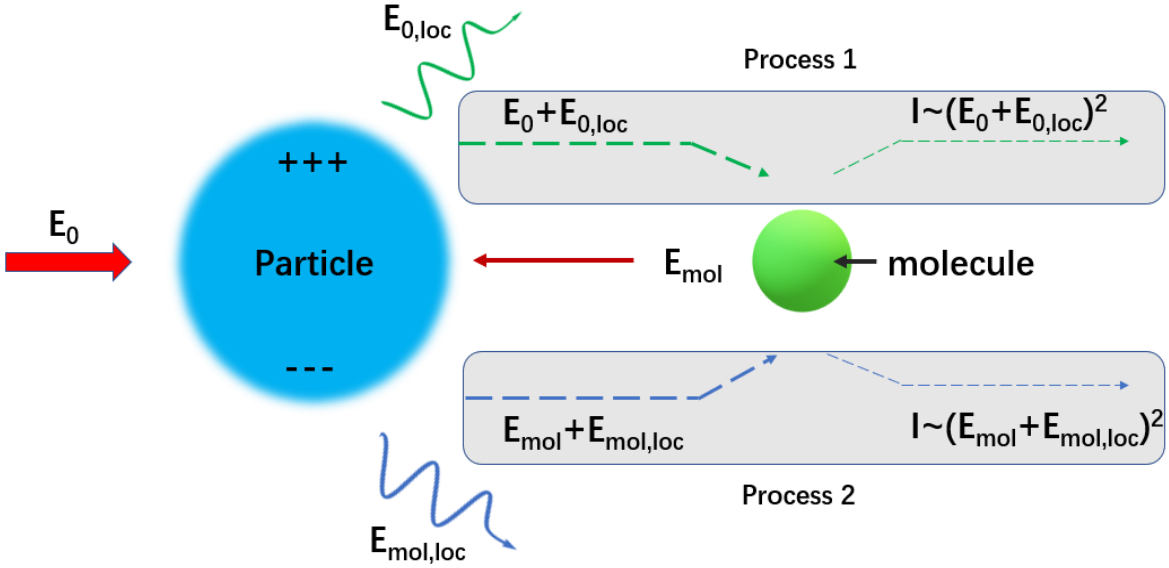

Figure 1.7 Schematic showing the electromagnetic (EM) effect for SERS enhancement using the two-processes mechanism.

Another contribution to the enhancement factor already mentioned in the previous sections is the charge-transfer (CT) effect, which is widely accepted as part of the chemical enhancement (CE) mechanism. Enhanced Raman occurs when the excitation energy matches the requirement for a real electronic state. A similar enhancement effect can be observed in SERS and can be explained by the charge-transfer process, which considers the metal and the molecule systems as a whole. In that case, the charge is transferred from the metal surface with a wide electronic band to the quantum levels of the adsorbed molecule[30]. The Fermi level of the metal is considered to lie between the molecular ground state level and an electronically excited level. Hence, a metal can promote charge transfer to the adsorbate when excited with the appropriated laser energy, leading to an increase in the Raman Signal.

The CT mechanism requires the analyte and metal to be close enough to allow for a sufficient overlap of their wave functions, also, it has strict requirements for the geometry,

bonding, and molecule energy level.[31] As a result, it is not normally dominant in most SERS cases and it is considered an additional explanation for the EM mechanism.

1.3.4 SERS Substrates

SERS is a surface technique, and the preparation of suitable surfaces that support the effect is important for its application. As discussed above, metallic nanostructures are used as SERS substrates since they can support strong surface plasmon resonances. A good SERS substrate must provide both uniformity and high field enhancement. In general, structures made of gold or silver are most widely used in SERS applications because they have the right optical properties to obtain a strongly localized surface plasmon in the most interesting range for SERS (~400-1000 nm).

Three main classes of substrates are widely applied in SERS studies. They include a metallic electrode, metallic nanoparticles in suspensions, and 'planar' metallic structures.[32]

1.3.4.1 Roughened electrode surface

As mentioned in Section 1.3.1, the first observation of the SERS phenomenon was from an electrochemically roughened silver. Metallic electrodes have been crucial in the development of the SERS method since SERS originated in electrochemistry.

Electrochemical roughening techniques, such as oxidation-reduction cycles (ORCs), are often utilized to prepare the uniformly roughened electrode surface for SERS. The application of ORCs is referred to as SERS activation. Section 2.2 presents the experimental procedures for preparing the metallic electrode in more detail.

1.3.4.2 'Planar' nanostructured metallic surface

The most common method for performing a SERS experiment is dropping a liquid sample on a metallic nanostructure (normally silver or gold) supported by either a silicon or a glass surface. With the development of technologies for nanofabrication, a whole new range of ordered planar metallic structures has been studied for SERS, such as organized arrays of metallic nanoparticles. The experiment processes developed by Nicolas[33] *et al*. provide an example for the fabrication of arrays of inverted pyramids. More detailed information can be found in Ref. 27.

1.3.4.3 Metallic nanoparticles in suspension

Colloidal suspensions are a frequent example of metallic nanoparticles dispersed in liquids. In contrast to the two traditional SERS substrates described previously in sections 1.3.4.1 and 1.3.4.2, colloidal suspensions of silver or gold are easy to synthesize in the laboratory. Thus, numerous researchers became interested in realizing SERS by using colloids. For instance, the first single-molecule SERS detection was accomplished using metallic colloids suspended in water[34] or deposited on a planar substrate.[35]

1.3.5 Electrochemical Surface-Enhanced Raman scattering (EC-SERS)

Researchers have always been interested in the combination of electrochemical techniques with SERS measurements, called electrochemical surface-enhanced Raman scattering (EC-SERS).[36] The EC-SERS approach has been dubbed the most difficult SERS technique, due to the fact that both electromagnetic (EM) and chemical enhancement (CE)

occur on the electrode surface. Chemical enhancement contributes significantly to the Raman enhancement effect by facilitating chemisorption and charge transfer (CT) between the metallic electrode surface and the adsorbate.

One critical feature of EC-SERS is that it can detect the frequency shift and relative strength of spectral bands caused by charge transfer (CT) effects. The SERS intensities are strongly dependent on the change of the applied potential. This is because the coverage and the adsorption orientation of the molecule might be affected by the change in the electrode potential.[37, 38]

With those specific features, EC-SERS can be very useful as an analytical tool for obtaining important information about the adsorbate, such as the nature of the chemical bonding with the metal surface and the molecular orientation. In our study, EC-SERS has used to analyze the electrochemical reaction of the *N*-heterocyclic carbenes at silver electrode surfaces.

1.4 NHC ligands on planar metallic surfaces as a robust platform for SERS

1.4.1 Self-assembled Monolayers (SAMs)

Self-assembled monolayer (SAM) describes the spontaneous assembly of organic molecules from either gas or solution phase onto the surface into semi- or fully- crystalline arrays.[39] The discovery of the self-assembly phenomenon can be traced back to 1946; Zisman *et al.*[40] reported that N-octadecylamine adsorbed from solutions in non-polar solvents forms self-assembled monolayers (SAMs) on a polished glass surface. Following

that, self-assembly technology evolved into a specialized monolayer formation technique that has been extensively investigated.

Compared with other monolayer technique, SAMs shows specific advantages, such as easy preparation, low cost, high degree of order, and good stability in various temperatures, solvents, and potentials.[41] The studies of SAMs have achieved rapid development in different areas over the last decade, including electrochemistry, biology, and molecular electronics.

Molecules used for the generation of SAMs are organic compounds with a head group, a tail (organic spacer), and a functional end group (Figure 1.8). SAMs are formed by the strong affinity between the head group and the substrate; therefore, the head group bind to the substrate from either the gas or solution phase.[39, 42, 43] The affinity can be interpreted either as a chemical bond or intermolecular interactions, such as van der Waals forces. Additionally, the most widely studied head group are thiols which are known to strongly bind to gold,[44-51] silver,[44, 46, 52] copper,[44] platinum,[53] and other metallic surfaces.[54, 55] Often, the head group is followed by a tail, also known as an organic spacer. The tail, typically an alkane chain, acts as a link between the head group at the substrate surface and the functional group at the other end of the molecule. A functional group connected to the opposite end of the tail provides the monolayer with various fabrication options and opportunities to tune its surface chemical properties.

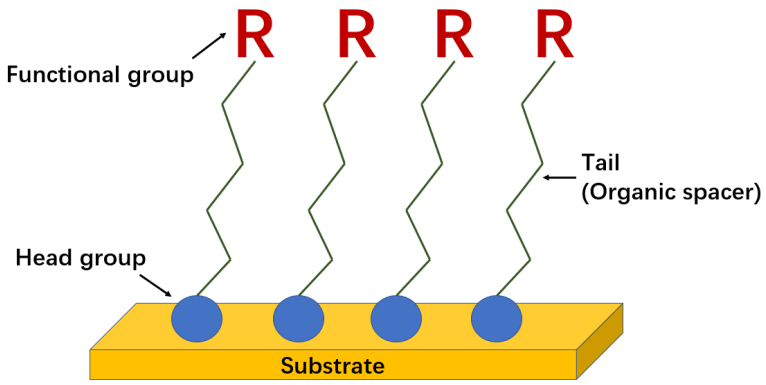

Figure 1.8 Schematic diagram of self-assembled monolayers (SAMs) on a metal surface

1.4.2 Thiols basic SERS substrates

SERS enhancement occurs through a surface-dependent process of field localization that quickly reduces away from the SERS-active surface. The Raman signal is increased only when the target analyte is immediately adsorbed on or extremely close to the SERS-active substrate.[23] SERS applications are often employed to directly detect target analytes, which are generally organic molecules having a strong surface affinity and detectable intrinsic Raman activity. On the other hand, SERS continues to experience difficulties investigating analytes with poor surface affinity or weak Raman activity, as well as establishing selective detections. In order to overcome this obstacle, novel surface chemistries on SERS active substrate must be developed. For instance, a variety of surface modification approaches is used to increase the analyte binding affinity to a SERS-active surface. Alkane thiol-based compounds are the most often used surface chemistries and modifications due to their ease of formation of SAMs on a SERS-active metal surface. While several chemical groups interact with noble-metal surfaces, thiols are almost

exclusively utilized as surface functionalized.[56] Their extensive application is owing to their great affinity for noble metals and their ability to spontaneously form a compact and well-defined monolayer.[39, 42, 56, 57]

However, the application of thiol-functionalized surfaces is severely constrained by (1) the stability of monolayers on the metal surface, particularly in biological environments or under harsh chemical conditions,[58] and (2) the difficulties associated with the synthesis of stable thiols, particularly without multiple protection and deprotection steps. Alternative surface functionalization strategies are required to solve these twin disadvantages in order to create robust and adaptable monolayer-based plasmonic sensors.

1.4.3 SERS substrates based on N-Heterocyclic Carbenes (NHC)

In the last two decades, NHCs have become one of the most extensively researched ligands in molecular chemistry, finding a variety of applications in the disciplines of catalysis and biochemistry.[59-62] Recent advances in materials chemistry have enabled the functionalization of surfaces, polymers, and nanoparticles using NHCs.[63]

Due to some challenges related to the applicability of thiols as modifiers in basic SERS substrates (for example, poor stability of the thiols-based monolayers on the metal surface and the difficulties with the synthesis of stable thiols), Joseph *et al*. recently investigated N-Heterocyclic Carbenes (NHCs) as a robust SERS platform. NHCs were shown to be resilient and capable of post-synthetic modification.[64] NHCs are heterocyclic compounds containing a carbene carbon and at least one nitrogen atom within the heterocycle.[65] The benzimidazolium peaks are SERS-enhanced and provide a signature for

the NHC SERS spectrum. Due to the ease with which functional groups with distinct vibrational modes in the quiet region (such as nitrile) may be added, these species are very desirable as tags for a range of SERS surfaces. In comparison to thiol ligands, NHC-coated on SERS-active gold film-over-nanosphere substrates (AuFONs) are resistant to a wide range of solvents, acids, bases, and reductants. Finally, the stability of NHC-coated AuFONs enables surface modification post-synthesis. These considerations, ranging from the simplicity of synthesis to better stability, suggest that NHCs have a strong potential to displace thiols in the near future for surface-enhanced spectroscopic applications.

As introduced in Section 1.3.4, Gold (Au) and silver (Ag) are most widely used for the preparation of SERS substrates due to their high stability and right optical properties to obtain a strongly localized surface plasmon in the visible/near-infrared exaction range (~400–1000nm) where most of the Raman scattering occurs.[32]

Previous work on the application of NHC in SERS focuses on the synthesis of the NHC monolayer on gold nanostructures.[64, 66] However, the NHC monolayer on silver nanostructures has never been studied as a SERS substrate and has a great potential study value since Ag and Au nanoparticles (NPs) have their own advantages and disadvantages in SERS. The main difference is the stability. Ag NPs have less stability compared with Au NPs. However, Ag NPs often provide much stronger plasmonic properties which give the higher enhancement factor and, therefore, offer stronger SERS signals than Au NPs.[67, 68] This research will focus on the study of silver nanostructured electrodes. With an Ag electrode, an electrochemical activation method can be processed to produce nanoparticle mental structure and to investigate the electrochemical stability of NHC adsorbed on the activated nanostructured Ag surface.

Chapter 2 - Experimental Details

2.1 Electrochemical Experiments

2.1.1 Electrolyte, Electrodes, and Cell

In these studies, a three electrodes system was used for each experiment. The Working electrode was made by a 99.9% silver rod. The silver rod was cut to a disc of 6.50 mm diameter and was placed in a Teflon tube. A stainless-steel rod was threaded into the hole in the back of the silver disk for the electrical contact (Figure 2.1). The counter electrode was a platinum wire with ~0.2 mm diameter. The reference electrode was a silver wire with ~0.2 mm diameter and coated with silver chloride.

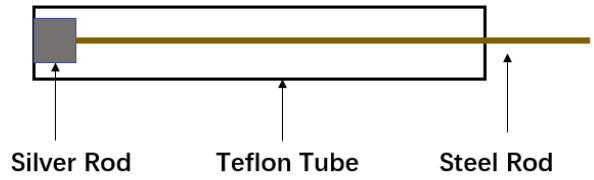

Figure 2.1 Schematic view of the working electrode design used in the electrochemical cell. A silver rod worked as the working electrode in a three electrodes system. The design is completed by three components: a silver rod, a Teflon tube, and a steel rod.

To prepare the reference electrode, a silver wire was coated with silver chloride. Firstly, a silver wire was cleaned by polishing with emery paper and was sonicated for 10 minutes in methanol and 10 minutes in ultra-pure water (18.2 MΩ cm resistivity from a Barnstead NANOpure Diamond water purification system). Next, another silver wire, used as the cathode, and the cleaned silver wire (anode) were immersed into the 0.1 M hydrochloride

acid and a 10mA current was passed for 1min. The electrode was then rinsed with ultra-pure water and stored in a 1 M potassium chloride solution.

The SERS electrochemical cell is shown schematically in Figure 2.2. The main body consists of two Teflon pieces, a steel top, and a glass window. Four screws on each side were used to secure all the parts together. The bottom Teflon part has a round hole with a 0.5-inch radius in the center. The top Teflon part has a round hole with a 0.25-inch radius in the center and another two holes are designed for both the reference electrode wire and the counter electrode wire, which are aside from the center hole. The two holes are going through from the bottom of the center hole to the top of the Teflon part. A rubber O-ring was put between the glass and the top cell part and another one was put between the bottom part and top part. When the two Teflon pieces were assembled with the screws, the top piece pressed against the bottom one and the glass cover pressed against the top piece through the O-rings to prevent the electrolyte leaks.

To set up the system, the reference electrode and counter electrode were inserted through the holes aside from the center hole and the working electrode was inserted through the hole in the center from the bottom Teflon piece (Figure 2.3).

0.1 M potassium chloride solution was used as the electrolyte. To make the 0.1 M potassium chloride solution, 0.745 g of potassium chloride salt was dissolved in 100 ml of ultrapure water using a 100 ml volumetric flask. All glassware and Teflon parts were cleaned in a 98% sulfuric acid bath for 24 hours before each experiment to get rid of any possible organic contamination and followed by sonication for 10 minutes in methanol and 10 minutes rinsing in ultrapure water to get rid of possible inorganic contamination.

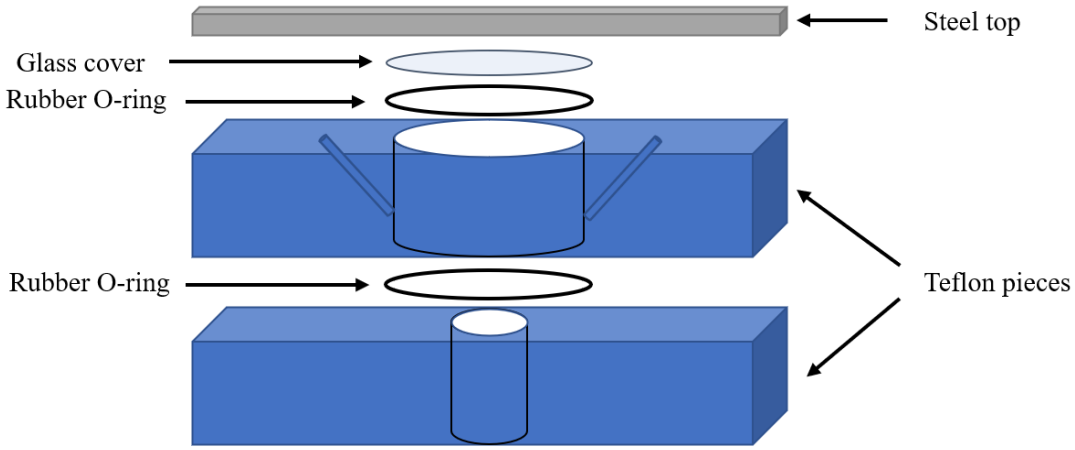

Figure 2.2 Schematic views of the electrochemical cell used in SERS experiments.

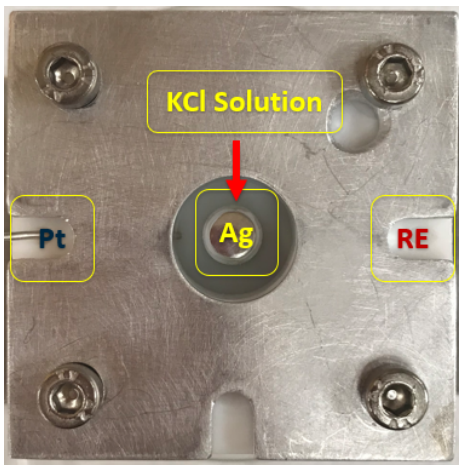

Figure 2.3 Top view of the electrochemical cell used in SERS experiments. Three electrode system was set up in the electrochemical cell. Left: counter electrode; Right: reference electrode; Middle: working electrode with potassium solution used as the electrolyte.

2.1.2 Preparation of the SERS-active Ag electrode surface.

Before each experiment, a freshly mirror-finish Ag working electrode was prepared by mechanical polishing with 600, 2400, and 4000 grit emery paper (Buehler), followed with successively 1, 0.3, and 0.05 μm alumina suspensions (Buehler). The electrode was then sonicated for 10 minutes in methanol and 10 minutes in ultrapure water before immersion into the electrolyte.

It is known that in order to make the Ag electrode surface ready for SERS, the surface needs to be roughened with an electrochemical pre-treatment procedure. This procedure is also called "activation".[69, 70] In the activation procedure, a few oxidation-reduction cycles (ORCs) were performed in 0.1 M potassium chloride electrolyte. In these experiments, three cycles of triangular potential sweeps with the potential from -700 mV to +500 mV at a scan rate of 5 mV/s were applied to the clean polished mirror-finish Ag electrode in order to obtain the desirable roughness.

Figure 2.4 shows the surface change under the oxidation-reduction cycles of the polished Ag working electrode surface whereas Figure 2.5 shows a cyclic voltammogram obtained during an activation cycle. The arrows indicate the potential starts from -800 mV to +500 mV and back to -800 mV. At potentials more positive than +50 mV, the polished silver surface is oxidized, forming an insoluble AgCl product that deposits onto the silver surface forming a black film (Fig. 2.4 b). During the reverse scan, the AgCl film is reduced back to metallic silver (Fig. 2.4 c) and is naturally roughed. Typically, after three oxidation-reduction cycles (ORCs), a desired natural roughness is produced.

Figure 2.6 is the scanning electron micrograph of a silver surface fabricated by the ORCs described above. The nodule width of the roughened Ag electrode has been shown to correlate with the SERS efficiency of the activated substrate.[69, 71] Different fabrication of SERS substrates can affect the shape and size of the nanoparticles and, hence, affect the enhancement of SERS signals.[72, 73] The SEM micrograph in Fig. 2.6 indicates that the freshly formed silver surface is evenly roughed with a nodule width of about 500 nm. This feature size is among the optimum to provide a significantly enhanced Raman signal for a variety of analytes.[69, 70]

Figure 2.4 Surface appearance when oxidation-reduction cycles (ORCs) are applied during the activation procedure.

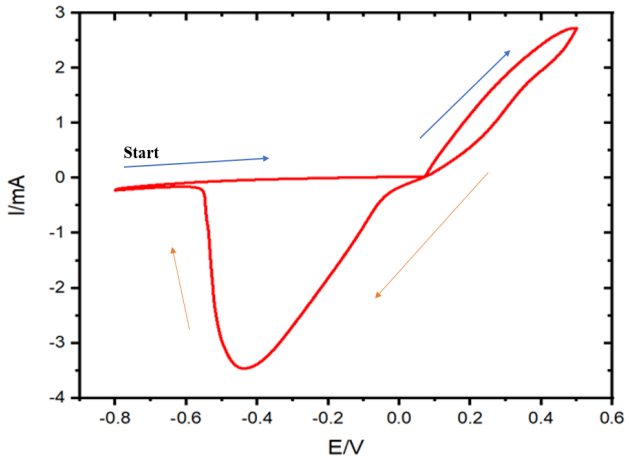

Figure 2.5 Cyclic voltammetry of activation procedure. Arrows indicate that the potential goes from -800 mV to +500 mV and back to -800 mV.

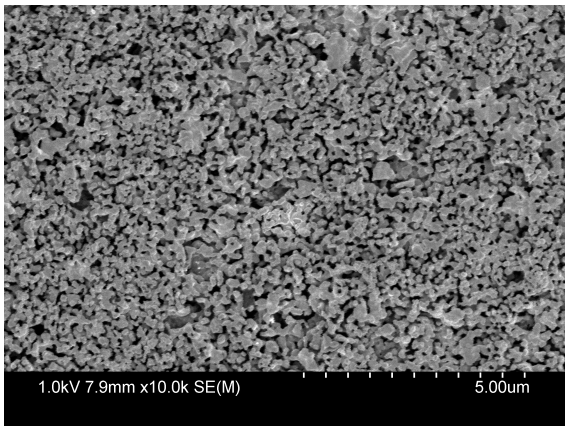

Figure 2.6 Scanning electron micrograph of an Ag surface fabricated by ORCs.

2.1.3 Deposition of NHC self-assembled monolayer

Two kinds of benzimidazolium *N*-heterocyclic carbenes (NHCs) functionalized silver surfaces were studied. The *N*-heterocyclic carbenes (NHCs) adducts were synthesized by Ishwar Singh from Dr. Cathleen Crudden's research group (Queen's University). The structures of the NHC adducts are shown in Figure 2.7. They are a 1,3-diisopropyl-benzimidazolium triflate salt (Fig. 2.7a) and 1,3-diisopropyl-5,8-phenyl-benzimidazolium bicarbonate salt (Fig. 2.7b).

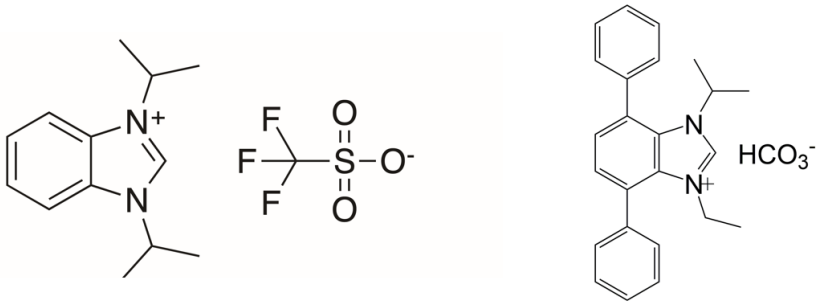

NHC Triflate Salt NHC Carbonate Salt

Figure 2.7 Molecular schematic of 1,3-diisopropyl-benzimidazolium, (a), triflate salt (left) and right is 1,3-diisopropyl-5,8-phenyl- benzimidazolium, (b), bicarbonate salt (right).

Self-assembled monolayers were prepared by immersion of the freshly activated silver electrode in a 10 mM solution of the corresponding bicarbonate or triflate salt in MeOH (HPLC grade) for 24 hours at room temperature. Following this, the silver electrodes were rinsed with methylene chloride, THF, and methanol (4 x 2 mL) and dried under a stream of argon.

2.2 Raman instrument

Figure 2.8 shows the schematic equipment setup for the SERS experiments. The spectroelectrochemical cell was fixed by a designed translational stage placed on the platform of the Renishaw 1000 Raman microscope. The three electrodes were connected to a BioLogic SP-300 potentiostat and interfaced to a PC operated by EC Lab/BT lab version 11.10 electrochemical software.

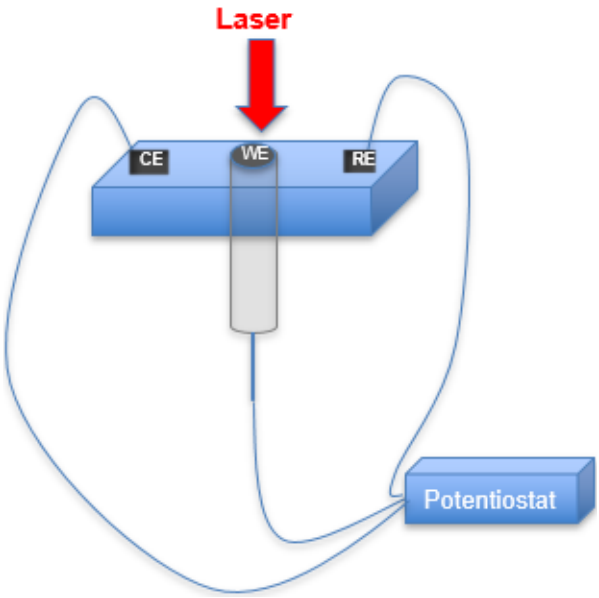

Figure 2.8 Schematic equipment setups for the SERS measuring experiments

SERS measurements (ranging from 400 cm^{-1} to 1800 cm^{-1}) were collected using a Renishaw inVia confocal Raman microscope system (Renishaw Inc., Hoffman Estates, IL) and interfaced to a PC operated by WIRE 4.4 software. The schematic setup for the Raman system is shown in Figure 2.9. Laser excitations at 633, 532, and 785 nm wavelengths were available in the system. A 50X long working distance objective was attached to the microscopy and used to focus the laser beam on the surface of the silver electrode. The beams were directed to the microscope objective by several optical elements and the back-scattered light was collected by the same objective lens. Then, the light was directed to the beam splitter filter, which allowed only the inelastic Raman scattering lights to pass through while the elastic Rayleigh scattering light was removed. After that, the light was directed to a diffraction grating and the Raman spectra were recorded by a CCD camera. Each spectrum was later analyzed by the WIRE 4.4 software available on the PC.

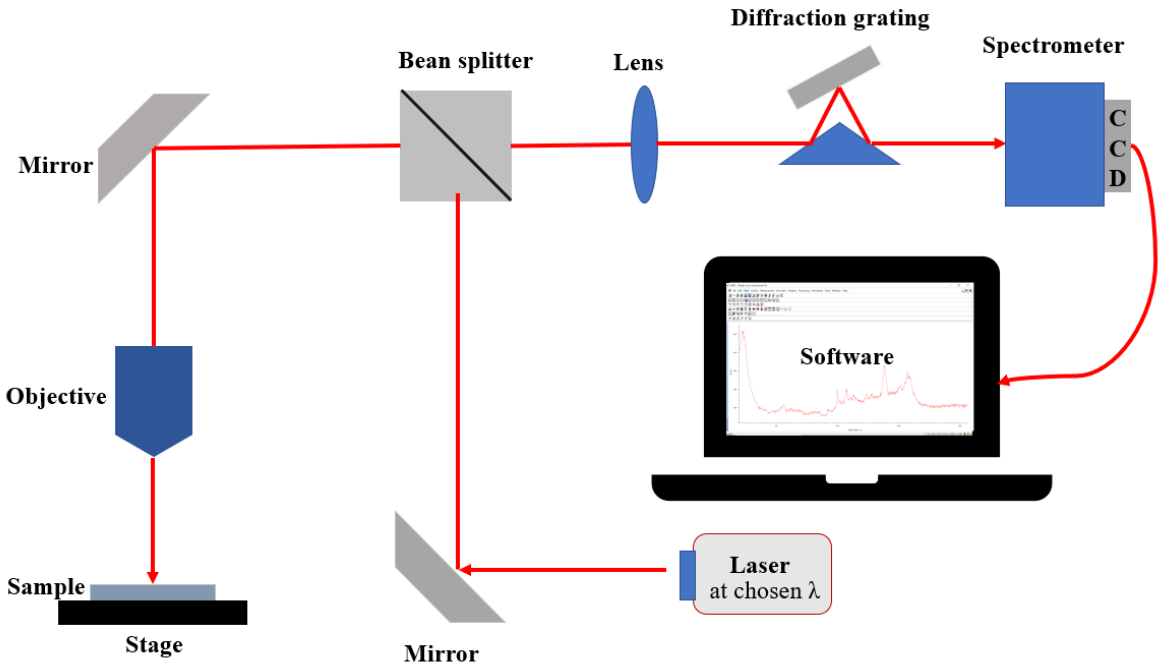

Figure 2.9 Block diagram showing the experimental setup of the Renishaw inVia Raman system used in the SERS experiments

2.3 SERS experiments

The appropriated laser (633, 532, and 785 nm wavelength) was turned on with the turnkey and the Raman instrument was allowed to warm up for one hour before each experiment. The Raman instrument was calibrated using a silicon standard with the main vibrational feature centered at ~520 cm^{-1}. Calibration was needed every time at the start of the instrument and the grating was adjusted to make sure that the intensity was uniform for each measurement.

2.4 Gaussian theoretical calculation

The theoretical molecular models were built using Gaussian View and calculated by the Gaussian16[74] program suite on Compute Canada. The molecular optimizations were carried out by density functional theory (DFT) methods to save time and computational resources. Due to the molecular have complicated structures, traditional methods such as Hartree-Fock (HF) show obvious errors in similar structures. However, the gold standard of computational chemistry, coupled-cluster methods (CCSD) costs lots of computational resources like processors and time. For the reasons mentioned above, the molecular optimizations were carried out by DFT (density functional theory), which provides good agreement with the experimental results and saves computational resources. The line shape of the simulated Raman spectra were determined with the Lorentz function and scaling was determined by the built-in function automatically. The molecule N-heterocyclic carbene (NHC) 1,3-diisopropylbenzimidazolylidene (BIz), and 3,6-biphenyl-1,3-diisopropylbenzimidazole (BP-BIz) were optimized preliminarily by the density functional method B3LYP and basis set 3-21G. After preliminary optimization, the B3LYP/3-21G optimized molecule structures were further optimized by B3LYP and 6-31G basis set. A tight conservative criterion (opt=tight command) was used for more accurate results.

Moreover, the polarization function and diffuse function were adopted by using 6-311+G and 6-311++G (d,p) basis sets. For the interaction between the molecules and the silver electrode, a single molecule approximate interaction was simulated by putting a silver atom near the molecule and calculating the molecular-silver model by DFT. However, the 6-31G, 6-311+G, and 6-311++G (d,p) basis sets are only suitable for elements between hydrogen and krypton. To cope with the silver atom, B3LYP/3-21G and

BPW91/LANL2DZ method/basis set combinations were adopted to calculate the molecular-silver The Raman spectra we atom system.re simulated by Gaussian View and then compared to the experimental spectra to help the assignment of the experimental peaks to vibrational modes.

This work is to carry out the DFT computations of 5-fluoro-uracil for the structural geometries, molecular charges, and vibrational frequencies using the DFT [B3LYP] method on the 6-311++G** basis set available in Gaussian-09 programs.[74] All normal vibrational modes have been assigned using the computed vibrational modes and related parameters are obtained from the Gauss View-5.09[75] of the Gaussian-09 program package.[74]

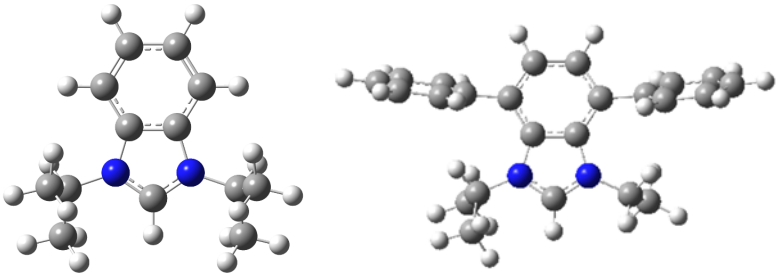

Figure 2.10 Gaussian calculated structure of BIz (left) and BP-BIz(right) ligand with a silver atom.

Chapter 3 - Results and discussion

3.1 Surface modification – NHC deposition on the silver surface

Figure 3.1 shows a comparison of the normal Raman of the protected N-heterocyclic carbene (NHC) 1,3-diisopropylbenzimidazolylidene (BIz) in solid-state and its SERS spectrum from a roughened Ag surface. BIz was adsorbed on Ag by self-assembly, where an activated (roughened) Ag electrode was immersed in a 10 mM BIz solution for 24 hours at room temperature. The surface was rinsed and dried after the adsorption and the SERS spectrum in Figure 3.1c was obtained after re-immersing the Ag electrode modified with BIz in 0.1 M KCl (the electrolyte used in the electrochemical measurements) at open circuit potential.

The measured vibrational frequency can be assigned to a specific normal vibrational mode by comparing the vibrational frequencies determined from the theoretical chemical calculation and experimental results. A DFT calculated spectrum of BIz (B3LYP/6-31G) is also presented in Fig. 3.1a. and the calculation comes from DFT in a simple environment, so the agreement can be improved with more complicated surroundings. However, a complicated environment increases consuming of computational resources exponentially. The asterisks in Fig. 3.1b denote the Raman bands (at 567, 781, 1024 cm^{-1}) of the triflate ($CF_3SO_3^-$) counter ion of the solid compound. A list of the calculated vibrational wavenumbers assigned with the corresponding vibrational modes and pictures are compared with the Raman and SERS wavenumbers in Table 3.1.

The SERS spectrum shown in Figure 3.1c agrees well with previous SERS results for BIz adsorbed on the Au surface.[76] The SERS bands at 1290 cm^{-1} and 1402 cm^{-1} are in

accordance with the features observed at 1310 cm^{-1} and 1420 cm^{-1} on Au surfaces[77]. The DFT-calculated vibrational modes for these bands show dominant contributions from the breathing of the benzimidazolium for the features around 1300 cm^{-1}, while vibrational motions of the isopropyl substituent play a larger role in the 1420 cm^{-1} region. Both characteristic bands shift slightly (~10 cm^{-1}) compare with the experimental spectra which indicate that the experimental spectra agree with the theoretical spectra well. An interesting feature of the SERS spectrum on the Ag surface, compared to Au surfaces, is the presence of a relatively strong feature at ~1600 cm^{-1} (Figure 3.1). That feature is assigned to benzene ring stretching (ν CC) (Table 3.1) and it also only shifts slightly (~10 cm^{-1}) upon adsorption.

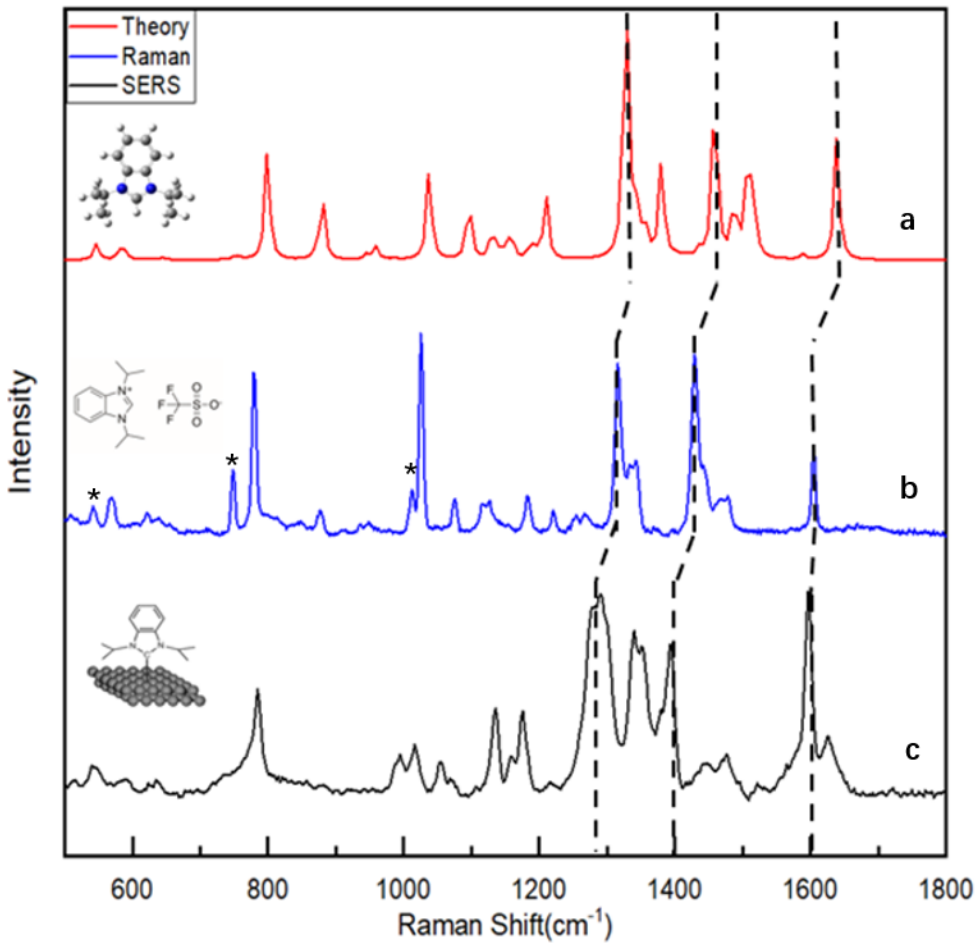

Figure 3.1 a) calculated Raman spectrum (DFT-B3LYP/6-31G) of benzimidazole; b) Raman spectrum of the solid benzimidazole N-heterocyclic carbene (BIz) protected by a

triflate counter ion. The asterisks (*) indicate the bands assigned to the triflate. The spectrum was obtained using 785 nm excitation and 10s acquisition time; c) SERS spectrum of BIz adsorbed on a roughened Ag electrode at open circuit potential. The electrode was immersed in 0.1 M KCl. The spectrum was obtained using 633 nm excitation and 1s acquisition time.

ν_{Cal} (cm^{-1})	ν_{Solid} (cm^{-1})	ν_{SERS} (cm^{-1})	Assignment	**Normal coordinate diagram**
799	781	784	ν(CN,CC,CH)Bz	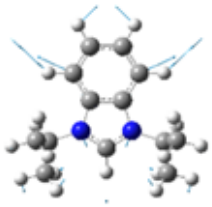
1037	1025	1016	ν(CC)Ar	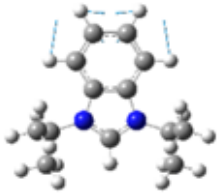
1096	1077	1057	ν(CC,CN)im+ φ(CH,CH3)iPr	
1209	1185	1173	ν(CC,CN)Bz,ipr+ φ(CH3)ipr	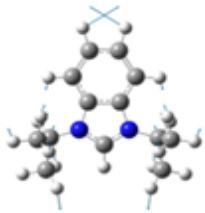
1327	1315	1289	ν(CC,CN)Br,Bz	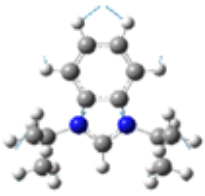

1458	1429	1392	ν(CN,CC)Bz+ φ(CH)Ar,iPr	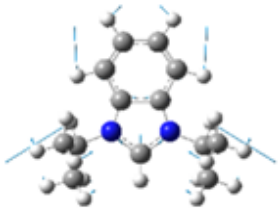
1638	1604	1598	ν(CC)Ar	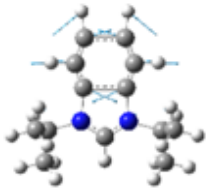

a ν: stretching; φ: bending out-of-plane; δ: bending in-plane Br: breathing mode; Bz: benzene ring; ipr: isopropyl group; Ar: aromatic ring; im: imidazolium ring

Table 3. 1 Calculated Raman wavenumbers (DFT-B3LYP/6-31G), along with the measured Raman and SERS band positions for BIz with the vibrational mode assignments and corresponding normal coordinate diagram.

Figure 3.2 compares the calculated spectra of 3, 6-biphenyl-1,3-diisopropylbenzimidazole (BP-BIz) and the solid Raman of the equivalent NHC 1,3-diisopropylbenzimidazolylidene protected with bicarbonate to the SERS spectrum of BP-BIz adsorbed on a roughened Ag electrode in 0.1 M KCl (same adsorption conditions as in Fig. 3.1). The main features in the SERS spectrum of the BP-BIz (Fig. 3.2c) appeared at (in cm^{-1}) 1002, 1030, 1178, 1299, 1390, 1444, and 1600. A list of the calculated vibrational wavenumbers assigned with the corresponding vibrational modes and pictures are compared with the Raman and SERS wavenumbers in Table 3.2.

The SERS bands at 1299 and 1390 cm^{-1} in Figure 3.2c, assigned by DFT to the ν (CC+CN) of the imidazolium ring and to ν(CN)im+φ(CN)iPr (Table 3.2), are clearly red-shifted relative to the normal Raman counterpart in the solid presented in Fig. 3.2b (dashed

line). A similar shift was observed in Fig. 3.1(black dashed line) for the bands in the same spectral region and assignments. Those red shifts (from the protected carbene in the solid to the adsorbed species onto Ag) in Figs. 3.1 and 3.2 are due to the electron-donating effect of the metal surface that affects the conjugation of the benzimidazolium system. This shift confirms the adsorption of NHC species to the Ag surface. The red-shifts relative to the protected carbene, shown in Figs. 3.1 and 3.2, are comparable to the observed from the SERS of NHC monolayers formed on Au surfaces .[64]

The adsorption of imidazole and benzimidazole carbene adducts on gold surfaces yielded characteristics SERS bands at 1288 and 1397 cm^{-1}, which agrees well with the red-shifted peaks observed in Figures 3.1 and 3.2.[64]

DFT calculations of the NHC species adsorbed on Au clusters showed that the relative intensity of the band around 1397 cm^{-1} is strongly dependent on the interaction of the alkyl side chains with the metal surface.[64] A list of the calculated vibrational wavenumbers assigned with the corresponding vibrational modes and pictures are compared with the Raman and SERS wavenumbers for BP-BIz in Table 3.2. In Figure 3.2c, the band in that region (~1390 cm^{-1}) is weaker and broader than observed in Fig. 3.1c and from previous SERS experiments using gold films.[64] The broadening in that region can be assigned to a convolution of configurations of the side chain relative to the silver surface.

Theoretical calculations for the adsorption of BIz on Au clusters revealed a strong effect of the position of the isopropyl groups on the relative intensities of the SERS bands, particularly for the 1400 cm^{-1} region, leading to the conclusion that the molecular adsorption involved a mixture of different conformations of the adsorbed species.[64]

The intensity and width of the ~ 1390 cm^{-1} band at the Ag surface (Fig. 3.2c) are further

affected by at least two factors. Firstly, the BP-BIz was adsorbed onto the Ag electrode surface from aqueous solutions containing chloride ions. This means that the interface structure is complicated by the co-adsorption of the chloride anions and solvent, which might keep the alkyl chain from interacting closely with the surface. Secondly, the presence of the phenyl rings in BP-BIz affects the Raman activity across the molecule leading to differences in that spectral range between the SERS features shown in Figs. 3.1c and 3.2c.

In the particular case of BP-BIz, the DFT calculations confirm that the alkyl modes are weaker, and the phenyl rings are stronger than the unsubstituted BIz species. The spectral differences in that region can be directly observed even when the solid versions of the two species (Figs. 3.1b and 3.2b) are compared.

The black dashed lines in Fig. 3.2 emphasize vibrational modes that did not shift significantly due to the adsorption of BP-BIz on the Ag surface. A closer examination of the vibrational modes for those bands (at 1002, 1030, and 1600 cm^{-1}) obtained from the DFT calculations indicated that they are dominated by movements of the phenyl substituents. In fact, the positions of these bands are similar to what is observed in the normal Raman of mono-substituted benzene (ring breathing mode at 1000 cm^{-1}, δCH ring at 1030 $cm^{-1,}$ and νCC ring at 1600 cm^{-1}).[78]

SERS experiments of benzene adsorbed on Ag surfaces showed that the ring modes red-shift when the molecule adsorbs flat due to the interaction between the π system of the molecule and the metal.[79] The fact that the vibrations of the phenyl system were not affected by adsorption corroborates the suggestion that BP-BIz formed a monolayer through the interaction of the carbene center with the metal surface, resulting in an upright configuration with the imidazole moiety attached to the silver while the biphenyl moieties

of the molecule were kept away from the surface (as indicated in the inset of Figure 3.2).

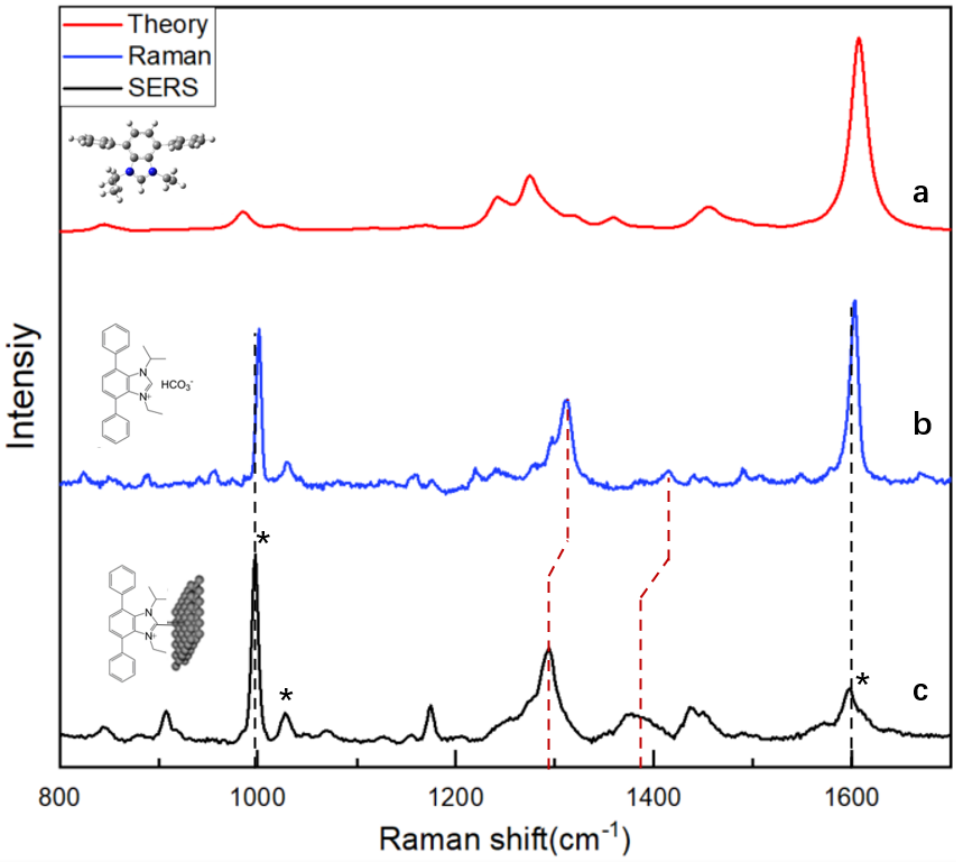

Figure 3.2 a) calculated Raman spectrum (DFT-B3LYP/6-31G) of 3, 6-biphenyl benzimidazole (BP-BIz); b) Raman spectrum of the solid BP-BIz N-heterocyclic carbene (BIz) protected by a bicarbonate counter ion. The asterisks (*) indicate the bands assigned to the phenyl substituent. The spectrum was obtained using 633 nm excitation and 1s acquisition time. c) SERS spectrum of BP-BIz adsorbed on a roughened Ag electrode at open circuit potential. The electrode was immersed in 0.1 M KCl. The spectrum was obtained using 633 nm excitation and 1s acquisition time.

ν_{Cal} (cm^{-1})	ν_{Solid} (cm^{-1})	ν_{SERS}(cm^{-1})	Assignment	Normal coordinate diagram
989	1001	997	ν(CC)ph+φ(CC)ph	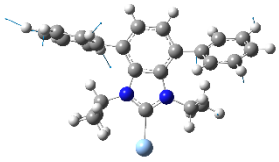
1027	1029	1028	δ(CH)ph	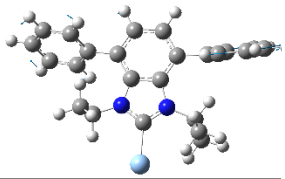
1265	1310	1294	δ(CH)Bz,ph+ν(CC,CN)im +φ(CH)iPr,et	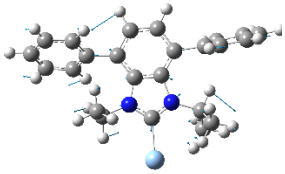
1606	1603	1598	ν(CC)Bz	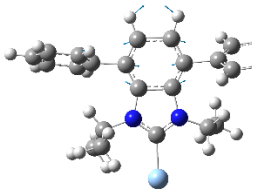

a ν: stretching; φ: bending out-of-plane; δ: bending in-plane Br: breathing mode; Bz: benzene ring; ipr: isopropyl group; Ar: aromatic ring; im: imidazolium ring

Table 3. 2 Calculated Raman spectrum (DFT - B3LYP/6-31G), along with the measured Raman and SERS band positions for BP-BIz with the vibrational mode assignments and corresponding normal coordinate diagram.

SERS spectra (Figure 3.3) of 1,3-diisopropyl-benzimidazolium (BIz) adsorbed on the gold surface have been measured by DeJesus *et al*. in 2018.[64] Peaks at ~1310 and 1420 cm^{-1} provide significant information of the molecule and can be considered the characteristic peak of BIz-Au. This information is used as the literature reference to compare with the theoretical and experimental spectrum in the future discussion of the assignments.

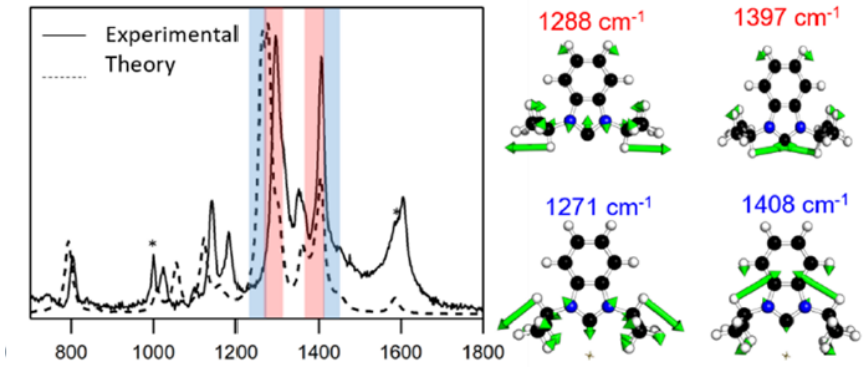

Figure 3.3 Experimental BIz-Au SERS spectra (solid) and theoretical SERS spectra (dashed) overlaid. Adapted from Ref. 1. Copyright American Chemical Society 2018.

3.2 NHCs modification in self-assembled monolayers in Ag surfaces

One of the main advantages of N-Heterocyclic Carbenes (NHCs) applications in self-assembled monolayers in Au surfaces is their stability. Stable NHC monolayers in Au have been demonstrated and those monolayers have endured very harsh conditions.[63, 80, 81] The stability of the monolayers was probed by a variety of methods.[82-84] The post-modification of the adsorbed monolayer on Au was successfully achieved and probed by SERS.[66]The results from Figures 3.1 and 3.2 show that similar NHC monolayers can be formed on Ag surfaces. However, the more effective catalytic characteristics of Ag (relative to Au) suggest a higher potential for degradation, particularly when the monolayers are formed from aqueous solutions. In fact, degradation evidenced by time-dependent spectral changes and variations in the spectral characteristics of the monolayers were observed for all NHC derivatives investigated here. Recently, a report on the adsorption of NHCs on oxidized copper surfaces revealed the reduction of the benzimidazolium ring to form urea,

formamide, and dimer derivatives (Scheme 3.1).[85] The presence of bis-carbene metal adsorbates in both Cu and Ag has also been observed by low-temperature scanning tunneling microscopy (STM).[86]The application of electrochemical SERS provides the potential to verify the formation of decomposition products of adsorbed NHC.

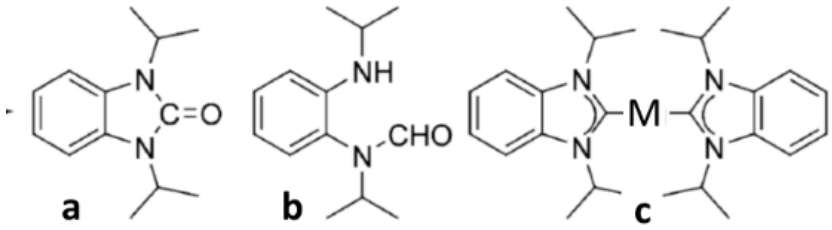

Scheme 3.1 Product for the reaction of NHC derivatives with a metal surface coated with oxides. a) urea derivative; b) formamide derivative; c) dimer derivative

The reactions of Ag_2O with imidazolium,[87] imidazolinium,[88] or benzimidazolium[89] can yield a large number of Ag- NHCs. According to some reports, metal-NHC complexes can decompose under certain conditions.[90-98] From the literature precedence, formamide and urea are observed as by-products of the *N*-heterocyclic carbene (NHC) monolayer formation when the NHCs are deposited on the silver surface.[99] Formamide forms as a result of NHC reacting with surface/lattice water, whereas urea forms when NHC reacts with silver oxide species. Scheme 3.2 shows the possible decomposition procedure of BIz(top) and BP-BIz(bottom). Benzimidazolium ring is opened to form Formamide when NHC reacts with surface/lattice water, whereas urea forms when NHC reacts with silver oxide species.

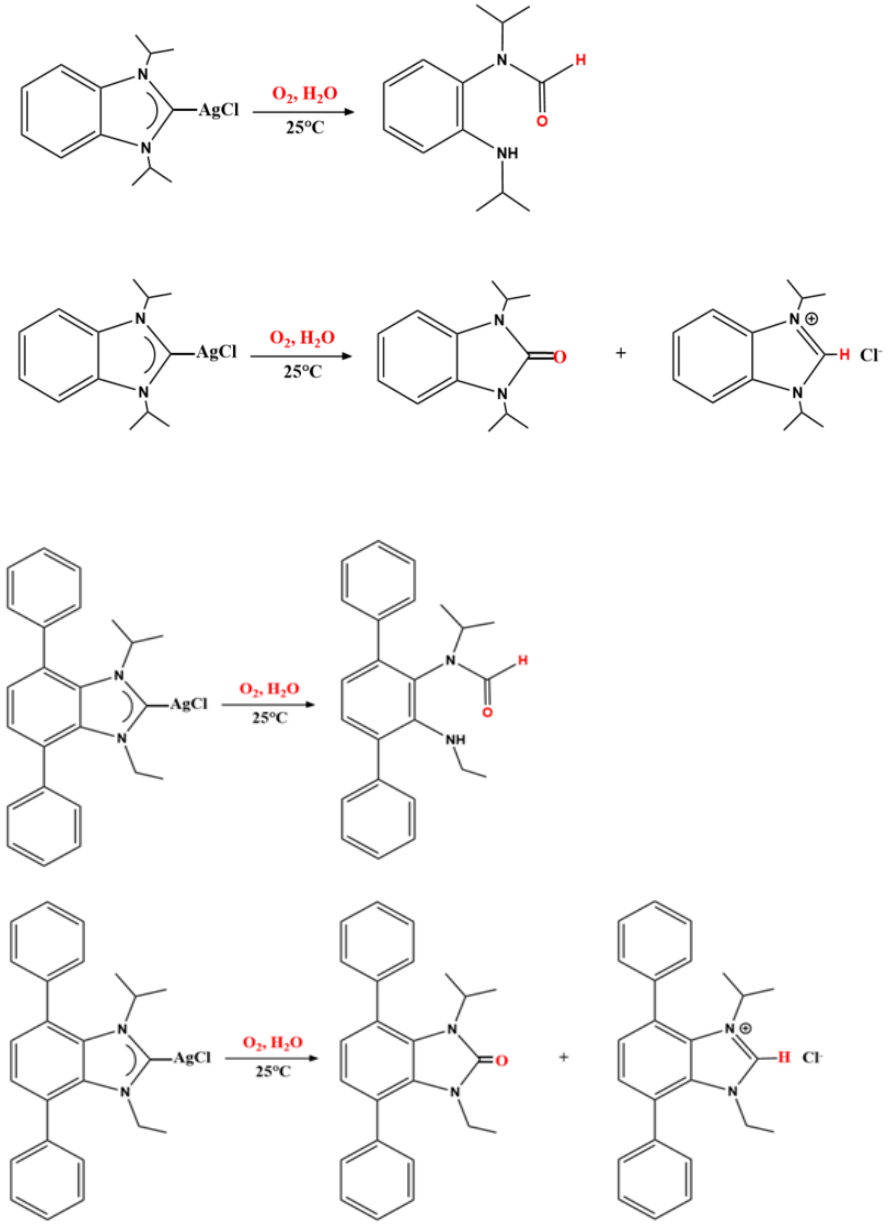

Scheme 3.2 Proposed decomposition of BIz(top) and BP-BIz(bottom). Benzimidazolium ring is opened to form Formamide when NHC reacts with surface/lattice water, whereas urea forms when NHC reacts with silver oxide species.

3.3 Investigation of the decomposed mixture on the Ag surface

Figure 3.4 shows the effect of the applied potential on the spectral characteristics of the BP-BIz adsorbed on a roughened silver electrode surface in 0.1 M KCl (the applied potentials were recorded against an $Ag/AgCl/Cl^-_{sat}$ electrode as described in the experimental section). As the applied potential is swept to more negative values, it is possible to observe the appearance of new bands, highlighted within dashed rectangles in Figure 3.4. These new SERS features should be related to the functionalization of the benzimidazolium ring, as reported in Ref. 77. The new vibrational features located at 1203, 1503, and 1578 cm^{-1} started to grow when the applied potential reached -400 mV (Fig. 3b). Although a variety of tests have been performed on the stability of NHC monolayers, their spectroelectrochemical behavior has not been explored yet. The potential for NHC reactivity in Cu and Ag surfaces is much higher than for Au because those are more reactive and typically covered by compound layers, such as oxides.[99] The products for the reaction of NHC-derived monolayers with copper oxide were identified by nuclear magnetic resonance (NMR) and they are presented in Scheme 3.1. All three compounds were present as a mixture at the metal surface and their relative yield from the decomposition depended on the conditions of the reaction and the initial state of the oxidized surface.[85]

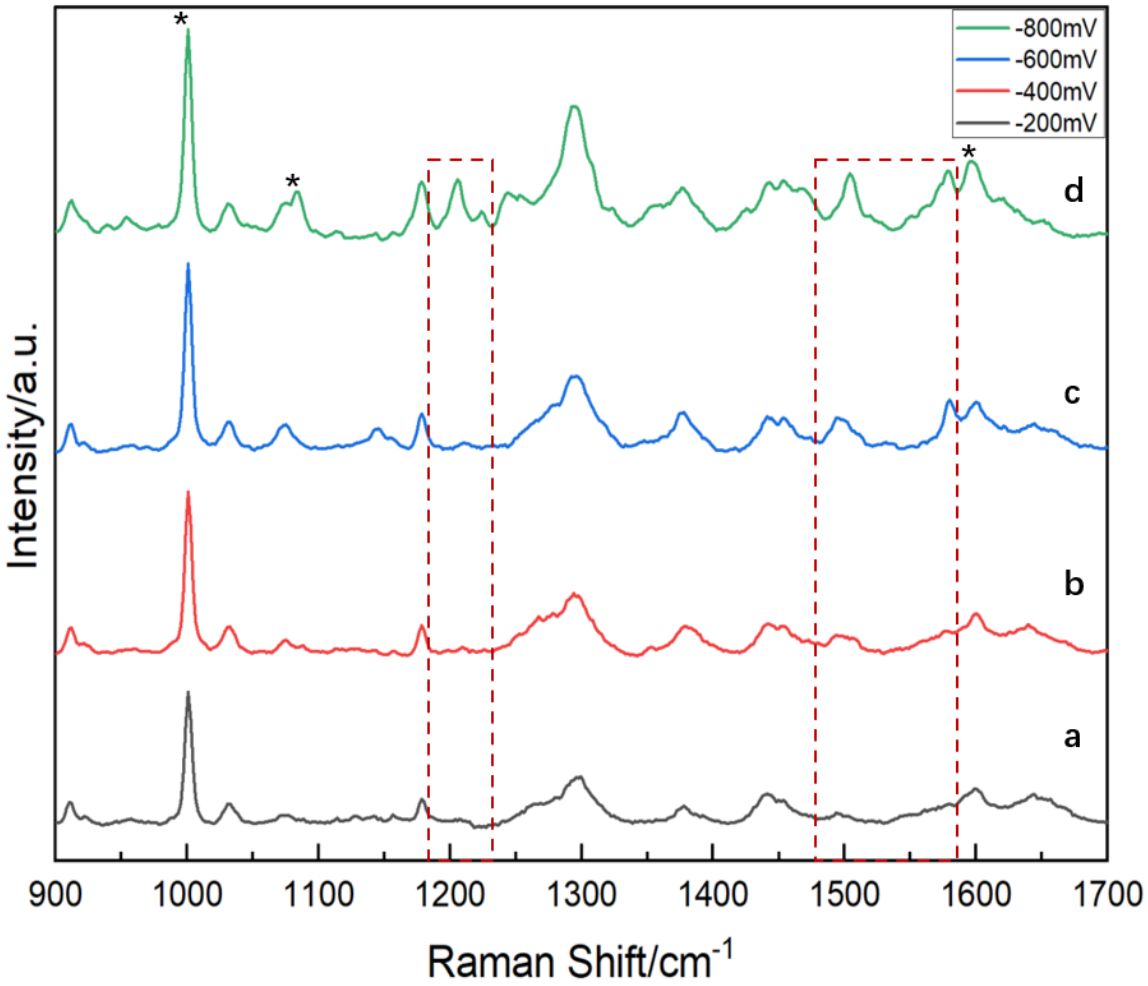

Figure 3.4 SERS spectrum of applied potential (-200, -400, -600, -800 mV) on the spectral characteristics of the BP-BIz.

In Figure 3.4, we can observe that the bands due to the phenyl substituents (marked with asterisks) do not shift as the potential becomes more negative. The relative intensities in Fig. 3.4 are also potential-dependent. Intensity changes in electrochemical SERS are not easy to interpret, due to several competing effects. For instance, the presence of potential-modulated charge-transfer contributions has been extensively investigated.[86] The intensity of SERS bands in the electrochemical environment depends on the energy gap between the (potential dependent) Fermi level of the metal and the molecular HOMO (or LUMO)

orbital. The intensities maximize once that energy gap matches the energy of the excitation laser.[100] Other factors that affect the absolute intensity of potential dependence of SERS bands in electrochemical conditions include the potential induced changes in surface coverage of adsorbates and counter ions.[101] On the other hand, relative intensity changes can be used together with the SERS selection rules to produce information about molecular orientation.[102] In the particular case of Figure 3.4, DFT calculations suggest that the strong band at 1295 cm^{-1} can be assigned to ν (CC, CN) im+φ(CC)iPr (Table 3.2) and it is characteristic of the imidazolium moiety. The relative intensity between the 1000 cm^{-1}-band assigned to the phenyl substituent and the 1295 cm^{-1}-band (I_{1000}/I_{1295}) varies from 3.9 at -200 mV to 1.6 at -800 mV. One possible interpretation of an increase in the relative intensity of the characteristic mode of the imidazolium part of the molecule (relative to the phenyl) is related to the potential-driven interfacial charge distribution. At -200 mV, the Ag surface is positively charged, and chloride ions are expected to be co-adsorbed with the organic species.[103] As the potential becomes more negative, the surface charge gradually changes, and the chloride ions start to leave the surface as the applied potential approaches the point-of-zero charge (pzc). This is a classical behavior that has been confirmed by several spectroscopic and electrochemical methods.[104, 105] The imidazolium end of the molecule then has a chance to approach the surface, leading to an increase in SERS intensity relative to the phenyl mode. Notice that the phenyl mode also gets closer to the surface as the whole molecule approaches due to the lower concentration of co-adsorbed chloride ions, however, the effect is the SERS intensity is more dramatic for the parts of the molecules in close contact, since the surface plasmon field decays exponentially from the surface.[106, 107]

The fact that the bands assigned to the phenyl substituents (marked with asterisks in Fig. 3.4) do not change position (and even absolute intensity) as the potential is moved to more negative values seems to indicate that the phenyl rings do not interact directly with the surface, even when the applied potential is very negative (-800 mV). We can then conclude that the phenyl part of the molecule did not change orientation relative to the surface, implying that the whole molecule remains upright even as BP-BIz undergo speciation at negative potentials (indicated by the appearance of new bands in Figs. 3.4b-3.4d). The same observation is valid for the imidazolium regions of the molecule (the 1295 cm^{-1} did not change position significantly with the applied potential). This implies that the speciation happened without breaking the ring. One of the characteristic new bands that are formed at potentials more negative than -400 mV is at ~1500 cm^{-1}. That band can be assigned to vibrations involving a functionalized NCN structure. Other new bands at 1203 and 1578 cm^{-1} can also be assigned to movements from the imidazole ring that shifted due to functionalization. The potential-dependent changes in the vibrational then indicate that the imidazolium region of the ring did not open, but functionalization was achieved in the NCN end of the molecule. The speciation of NHC in metal surfaces covered with oxides led to a urea derivative, indicated in scheme 3.1, that would fulfill these requirements.[85] However, the formation of an oxidation product (urea derivative) at more negative potentials presents a contradiction to this hypothesis. This can be rationalized by considering that in 0.1M KCl the Ag surface is always covered by a chloride layer at more positive potentials. In that case, the BP-BIz NHC interacts with a surface protected by a chloride layer acting as the counter-ion. At -400 mV, the coverage of chloride ions decreases, offering the NHC access to the remaining silver oxide species. The presence

of the urea derivative was further confirmed by comparing the SERS at -800 mV with the normal Raman of the solid urea derivative synthesized independently. The solid compound presented strong features at 1242, 1492, and 1620 cm^{-1} (Figure 3.5) which is in reasonable agreement with the discussion above. The main spectral characteristics of the speciation product did not change even when the potential was either moved to the hydrogen evolution region (~-900 mV) or more positive values (back to -200 mV).

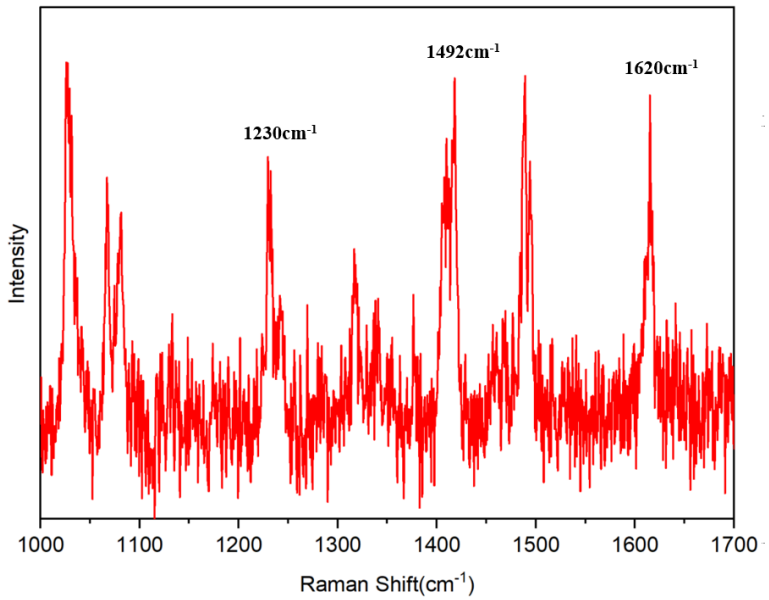

Figure 3.5 Raman spectrum of urea solid sample which shows strong peaks at 1230, 1492, and 1620 cm^{-1}.

Compared to BP-BIz, the SERS behavior under applied potential was very different for the BIz compound. Figure 3.6 shows the spectrum of adsorbed BIz obtained at different potentials. It is possible to observe immediately from Fig. 3.6 that several new bands are present under applied potential (compare the spectra from Fig. 3.1 to Fig. 3.6), indicating

fast speciation of the adsorbed NHC. The strongest features at -200 mV (Fig. 3.6a) are present at 1148, 1269 and 1503 cm^{-1}.

A clear red-shift is observed for these 3 bands as the potential moves to the negative direction and reaches -800 mV. Other prominent peaks also present potential-dependent changes in intensities and positions, particularly the bands between 1350 and 1451 cm^{-1} and the modes at 1567 and 1615 cm^{-1} (all included within the dashed rectangle regions in Fig. 3.6). New weak peaks appear when the potential reaches -600 mV at 1113, 1170, and 1312 cm^{-1} (marked with asterisks in Fig. 3.6). The behavior presented in Fig. 3.5 is much more complex than in Fig. 3.4. The only difference between the adsorbates in Figs. 3.4 and 3.5 is the presence of the biphenyl substituent in BP-BIz. The bulk substituents led to less packing at the surface and the SERS data in Fig. 3.4 suggests that the molecule remained upright during the potential sweep. In that case, only the imidazolium region of the molecule seems to be amenable to functionalization.

The situation in Fig. 3.6 implies a much more complex decomposition that potentially led to a mixture of products at the electrode surface. The Raman features in Fig. 3.6 can be linked to amine (e.g., ~1150 cm^{-1}), amide (e.g., ~1600 cm^{-1}), and hydrocarbon (~1430 cm^{-1}) functionalities. The characteristic NHC mode at ~1300 cm^{-1} is not present until the potential reaches -400 mV. The dependence on the peak positions points out to a stronger interaction of the adsorbate with the surface than observed in Fig. 3.4. The presence of a mixture of the speciation products described in scheme 1 cannot be ruled out, particularly due to the strong mode at 1500 cm^{-1} that can be correlated to the urea derivative and the bands in the 1400 cm^{-1} region that can be attributed to the formamide product indicated in Scheme 3.2. However, the absence of the characteristics NHC feature

at around 1300 cm^{-1} seems to suggest a more complete decomposition of the compound on the silver surface under applied potential, particularly at potentials more positive than -400 mV.

The lack of steric hindrance (as observed for BP-BIz) might also allow BIz to interact with the surface under a flat configuration, which would considerably change the position and relative intensities of the benzimidazole-related modes. In that case, the ~1300 cm^{-1}-band of the NHC could shift down to the 1269 cm^{-1}-band observed in Fig. 3.4. The magnitude of the shift would be comparable to what was observed for ring systems interacting with Ag surface in a flat configuration.[108, 109] In that case, the out-of-plane modes would be enhanced, which would significantly change the overall spectral pattern. However, a comparison of the expected enhanced out-of-plane modes obtained by DFT, indicated that bands at a lower frequency (less than 1000 cm^{-1}) should provide a significant contribution, which was not observed experimentally. Therefore, we conclude that the complex spectra in Fig. 3.6 are mainly due to speciation products, rather than simply orientation changes.

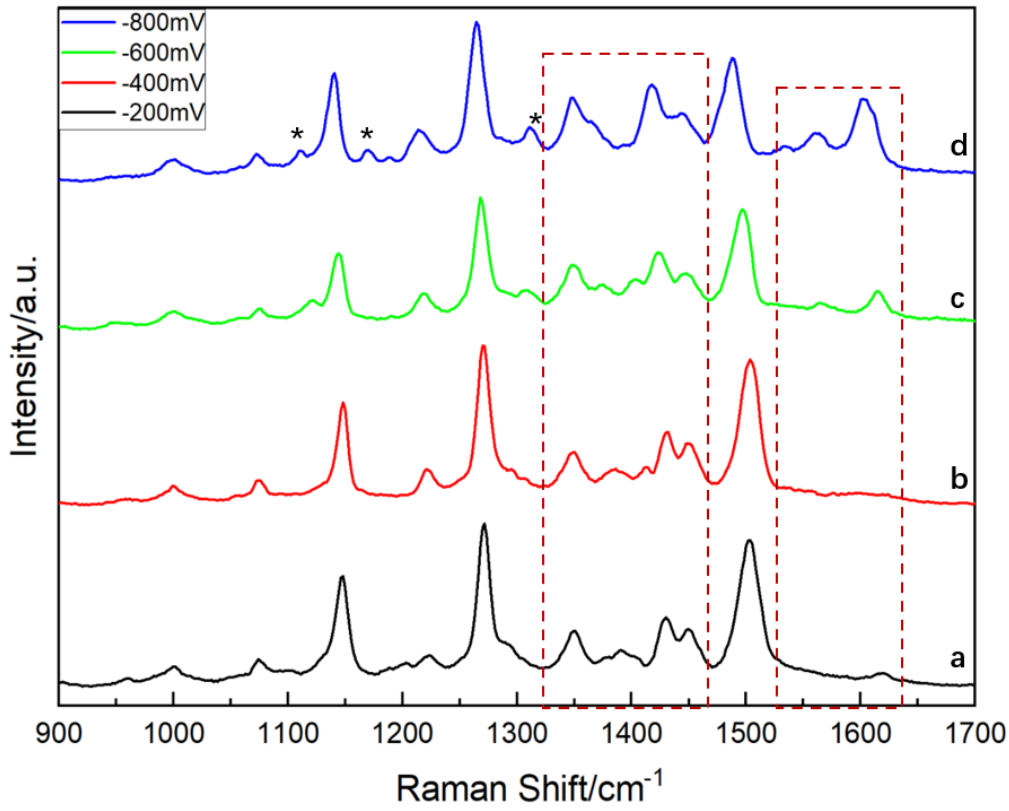

Figure 3.6 SERS spectrum of applied potential (-200, -400, -600, -800 mV) on the spectral characteristics of the BIz

3.4 Summary

The adsorption of NHC derivatives on a silver surface immersed in 0.1M KCl was investigated. The results demonstrated that an NHC derivative with bulky substituents in the benzene region of the molecule (BP-BIz) adsorb upright on a silver surface and it remains stable by interacting with a silver surface coated with chloride ions. As the chloride ions leave the surface, the carbene can then interact with oxides at the interface, generating mainly a urea derivative. The molecule remains upright even as it speciates. The speciation

product seems stable and remains at the surface when the potential is moved to values more positive than -400 mV. The situation is much for complex for an NHC compound with no substituents in the benzene part of the molecule. In this case, the molecule decomposed readily when mildly positive potentials (-200 mV) were applied. The decomposition product was complex and suggest a mixture of functionalities, including amine and amide species. The results presented here showed that NHC stability on the Ag surface is much more complex than for Au. This is in agreement with previous results that showed the decomposition of NHC molecules on Cu. These observations suggest that the use of NHC for the preparation of self-assembled monolayers on Ag and Cu surfaces should be considered carefully, particularly for experiments in aqueous solutions.

Chapter 4 - Conclusion

In this thesis, I studied the adsorption of NHC derivatives on a silver surface. The preliminary findings show that an NHC derivative (BP-BIz) with bulky benzyl substituents is able to be adsorbed vertically on a silver surface and stays stable by interacting with a silver surface covered with chloride ions. The carbene may then interact with oxides at the interface as the chloride ions depart the surface, resulting in a urea derivative. Even as it speciates, the molecule stays erect. When the voltage is adjusted to values more positive than -400 mV, the speciation product seems stable and persists at the surface.

For an NHC compound with no substituents on the benzene ring, the situation is even more complicated. When weakly positive potentials (-200 mV) were applied, the molecule disintegrated quickly. The complicated breakdown product includes amine and amide species, revealing that NHC stability on an Ag surface is much more complicated than on an Au surface. This is consistent with prior findings that NHC molecules decompose on Cu.

Overall, this project demonstrates that using NHC to build self-assembled monolayers on Ag and Cu surfaces should be carefully considered, especially for investigations in aqueous solutions. We may be able to get a better Ag surface for the NHC in the future by carefully constructing new NHC structures.

References

1. Smith, E.; Dent, G., Modern Raman spectroscopy: a practical approach. J. Wiley: Hoboken, NJ;Chichester, West Sussex, England;, **2005**.
2. Raman, C. V.; Krishnan, K. S., A New Type of Secondary Radiation. *Nature* **1928,** *121* (3048), 501-502.
3. Kneipp, K.; Moskovits, M.; Kneipp, H., Surface-enhanced Raman scattering: physics and applications. Springer Science & Business Media: **2006**; Vol. 103.
4. SVANBERG, S., " Biomedical Applications of Spectroscopy. *133*, 8.
5. Nijssen, A.; Koljenović, S.; Schut, T. C. B.; Caspers, P. J.; Puppels, G. J., Towards oncological application of Raman spectroscopy. **2009,** *2* (1-2), 29-36.
6. Rösch, P.; Harz, M.; Schmitt, M.; Peschke, K.-D.; Ronneberger, O.; Burkhardt, H.; Motzkus, H.-W.; Lankers, M.; Hofer, S.; Thiele, H. J.; microbiology, e., Chemotaxonomic identification of single bacteria by micro-Raman spectroscopy: application to clean-room-relevant biological contaminations. **2005,** *71* (3), 1626-1637.
7. Clark, R. J.; Dines, T. J., Resonance Raman spectroscopy, and its application to inorganic chemistry. New analytical methods (27). **1986,** *25* (2), 131-158.
8. Li, Z.; Deen, M. J.; Kumar, S.; Selvaganapathy, P. R., Raman spectroscopy for in-line water quality monitoring—Instrumentation and potential. **2014,** *14* (9), 17275-17303.
9. Palonpon, A. F.; Ando, J.; Yamakoshi, H.; Dodo, K.; Sodeoka, M.; Kawata, S.; Fujita, K., Raman and SERS microscopy for molecular imaging of live cells. *Nature Protocols* **2013,** *8* (4), 677-692.
10. Jablonski, A., Efficiency of Anti-Stokes Fluorescence in Dyes. *Nature* **1933,** *131* (3319), 839-840.
11. Haken, H.; Wolf, H. C., Molecular physics and elements of quantum chemistry: introduction to experiments and theory. Springer Science & Business Media: **2013**.
12. Demtröder, W., Laser spectroscopy: basic concepts and instrumentation. Springer Science & Business Media*:* **2013**.
13. Valeur, B.; Berberan-Santos, M. N., Molecular fluorescence: principles and applications. John Wiley & Sons: **2012**.
14. Massimi, M., Pauli's exclusion principle: The origin and validation of a scientific principle. Cambridge University Press: **2005**.
15. Schrödinger, E., An Undulatory Theory of the Mechanics of Atoms and Molecules. *Physical Review* **1926,** *28* (6), 1049-1070.
16. McCreery, R. L., *Raman spectroscopy for chemical analysis*. John Wiley & Sons: New York, **2000**; Vol. 157.;157;.
17. Sanderson, A. C.; University of Victoria. Surface-enhanced Raman scattering from a modified silver electrode (Doctoral dissertation). **2007**.
18. Ferraro, J. R., Introductory raman spectroscopy. Elsevier: **2003**.
19. Smith, E.; Dent, G., Modern Raman spectroscopy: a practical approach. **2005**.
20. Fleischmann, M.; Hendra, P. J.; McQuillan, A. J., Raman spectra of pyridine adsorbed at a silver electrode. *Chemical Physics Letters* **1974,** *26* (2), 163-166.
21. Jeanmaire, D. L.; Van Duyne, R. P.; electrochemistry, i., Surface Raman spectroelectrochemistry: Part I. Heterocyclic, aromatic, and aliphatic amines adsorbed on the anodized silver electrode. **1977,** *84* (1), 1-20.

22. Albrecht, M. G.; Creighton, J. A., Anomalously intense Raman spectra of pyridine at a silver electrode. **1977,** *99* (15), 5215-5217.
23. Moskovits, M., Surface-enhanced spectroscopy. **1985,** *57* (3), 783.
24. Langer, J.; Jimenez de Aberasturi, D.; Aizpurua, J.; Alvarez-Puebla, R. A.; Auguié, B.; Baumberg, J. J.; Bazan, G. C.; Bell, S. E.; Boisen, A.; Brolo, A. G., Present and future of surface-enhanced Raman scattering. **2019,** *14* (1), 28-117.
25. Kerker, M. J., Resonances in electromagnetic scattering by objects with negative absorption. **1979,** *18* (8), 1180-1189.
26. Kerker, M.; Siiman, O.; Wang, D., Effect of aggregates on extinction and surface-enhanced Raman scattering spectra of colloidal silver. **1984,** *88* (15), 3168-3170.
27. Kerker, M.; Wang, D.-S.; Chew, H., Surface enhanced Raman scattering (SERS) by molecules adsorbed at spherical particles: errata. **1980,** *19* (24), 4159-4174.
28. Wang, D.-S.; Kerker, M. J., Enhanced Raman scattering by molecules adsorbed at the surface of colloidal spheroids. **1981,** *24* (4), 1777.
29. Wang, D.-S.; Kerker, M. J., Absorption and luminescence of dye-coated silver and gold particles. **1982,** *25* (4), 2433.
30. Tsuneda, T.; Iwasa, T.; Taketsugu, T., Roles of silver nanoclusters in surface-enhanced Raman spectroscopy. **2019,** *151* (9), 094102.
31. Otto, A.; Mrozek, I.; Grabhorn, H.; Akemann, W., Surface-enhanced Raman scattering. **1992,** *4* (5), 1143.
32. Le Ru, E.; Etchegoin, P., Principles of Surface-Enhanced Raman Spectroscopy: and related plasmonic effects. Elsevier: **2008**.
33. Perney, N. M. B.; Baumberg, J. J.; Zoorob, M. E.; Charlton, M. D. B.; Mahnkopf, S.; Netti, C. M., Tuning localized plasmons in nanostructured substrates for surface-enhanced Raman scattering. *Opt. Express* **2006,** *14* (2), 847-857.
34. Kneipp, K.; Wang, Y.; Kneipp, H.; Perelman, L. T.; Itzkan, I.; Dasari, R. R.; Feld, M. S., Single molecule detection using surface-enhanced Raman scattering (SERS). **1997,** *78* (9), 1667.
35. Nie, S.; Emory, S. R. J. s., Probing single molecules and single nanoparticles by surface-enhanced Raman scattering. **1997,** *275* (5303), 1102-1106.
36. Wu, D.-Y.; Li, J.-F.; Ren, B.; Tian, Z.-Q., Electrochemical surface-enhanced Raman spectroscopy of nanostructures. **2008,** *37* (5), 1025-1041.
37. Gale, R. J., Spectroelectrochemistry: theory and practice. Springer Science & Business Media: 2012.
38. Tian, Z.-Q.; Ren, B.; Wu, D.-Y., Surface-enhanced Raman scattering: from noble to transition metals and from rough surfaces to ordered nanostructures. **2002,** *106* (37), 9463-9483.
39. Love, J. C.; Estroff, L. A.; Kriebel, J. K.; Nuzzo, R. G.; Whitesides, G. M., Self-assembled monolayers of thiolates on metals as a form of nanotechnology. **2005,** *105* (4), 1103-1170.
40. Bigelow, W.; Pickett, D.; Zisman, W., Oleophobic monolayers: I. Films adsorbed from solution in non-polar liquids. **1946,** *1* (6), 513-538.
41. Vos, J. G.; Forster, R. J.; Keyes, T. E., Interfacial supramolecular assemblies. Wiley Online Library: 2003; Vol. 8894.
42. Schwartz, D. K., Mechanisms and kinetics of self-assembled monolayer formation. **2001,** *52* (1), 107-137.

43. Schreiber, F. J., Structure and growth of self-assembling monolayers. **2000,** *65* (5-8), 151-257.
44. Laibinis, P. E.; Whitesides, G. M.; Allara, D. L.; Tao, Y. T.; Parikh, A. N.; Nuzzo, R. G., Comparison of the structures and wetting properties of self-assembled monolayers of n-alkanethiols on the coinage metal surfaces, copper, silver, and gold. **1991,** *113* (19), 7152-7167.
45. Nuzzo, R. G.; Allara, D. L., Adsorption of bifunctional organic disulfides on gold surfaces. **1983,** *105* (13), 4481-4483.
46. Walczak, M. M.; Chung, C.; Stole, S. M.; Widrig, C. A.; Porter, M. D., Structure and interfacial properties of spontaneously adsorbed n-alkanethiolate monolayers on evaporated silver surfaces. **1991,** *113* (7), 2370-2378.
47. Poirier, G.; Pylant, E., The self-assembly mechanism of alkanethiols on Au (111). **1996,** *272* (5265), 1145-1148.
48. Bain, C. D.; Whitesides, G. M., Molecular-level control over surface order in self-assembled monolayer films of thiols on gold. **1988,** *240* (4848), 62-63.
49. Biebuyck, H. A.; Bain, C. D.; Whitesides, G. M., Comparison of organic monolayers on polycrystalline gold spontaneously assembled from solutions containing dialkyl disulfides or alkanethiols. **1994,** *10* (6), 1825-1831.
50. Dubois, L. H.; Zegarski, B. R.; Nuzzo, R. G., Molecular ordering of organosulfur compounds on Au (111) and Au (100): Adsorption from solution and in ultrahigh vacuum. **1993,** *98* (1), 678-688.
51. Bain, C. D.; Evall, J.; Whitesides, G. M., Formation of monolayers by the coadsorption of thiols on gold: variation in the head group, tail group, and solvent. **1989,** *111* (18), 7155-7164.
52. Fenter, P.; Eisenberger, P.; Li, J.; Camillone III, N.; Bernasek, S.; Scoles, G.; Ramanarayanan, T. A.; Liang, K., Structure of octadecyl thiol self-assembled on the silver (111) surface: an incommensurate monolayer. **1991,** *7* (10), 2013-2016.
53. Li, Z.; Chang, S.-C.; Williams, R. S., Self-assembly of alkanethiol molecules onto platinum and platinum oxide surfaces. **2003,** *19* (17), 6744-6749.
54. Love, J. C.; Wolfe, D. B.; Haasch, R.; Chabinyc, M. L.; Paul, K. E.; Whitesides, G. M.; Nuzzo, R. G., Formation and structure of self-assembled monolayers of alkanethiolates on palladium. **2003,** *125* (9), 2597-2609.
55. Carvalho, A.; Geissler, M.; Schmid, H.; Michel, B.; Delamarche, E., Self-assembled monolayers of eicosanethiol on palladium and their use in microcontact printing. **2002,** *18* (6), 2406-2412.
56. Ulman, A. J., Formation and structure of self-assembled monolayers. **1996,** *96* (4), 1533-1554.
57. Vericat, C.; Vela, M.; Benitez, G.; Carro, P.; Salvarezza, R. J., Self-assembled monolayers of thiols and dithiols on gold: new challenges for a well-known system. **2010,** *39* (5), 1805-1834.
58. Schoenfisch, M. H.; Pemberton, J. E., Air stability of alkanethiol self-assembled monolayers on silver and gold surfaces. **1998,** *120* (18), 4502-4513.
59. Crudden, C. M.; Allen, D. P., Stability and reactivity of N-heterocyclic carbene complexes. **2004,** *248* (21-24), 2247-2273.
60. Hopkinson, M. N.; Richter, C.; Schedler, M.; Glorius, F., An overview of N-heterocyclic carbenes. **2014,** *510* (7506), 485-496.

61. Kantchev, E. A. B.; O'Brien, C. J.; Organ, M. G., Palladium complexes of N-heterocyclic carbenes as catalysts for cross-coupling reactions—A synthetic chemist's perspective. **2007,** *46* (16), 2768-2813.
62. Arduengo III, A. J.; Harlow, R. L.; Kline, M. J., A stable crystalline carbene. **1991,** *113* (1), 361-363.
63. Smith, C. A.; Narouz, M. R.; Lummis, P. A.; Singh, I.; Nazemi, A.; Li, C.-H.; Crudden, C. M., N-heterocyclic carbenes in materials chemistry. **2019,** *119* (8), 4986-5056.
64. DeJesus, J. F.; Trujillo, M. J.; Camden, J. P.; Jenkins, D. M., N-heterocyclic carbenes as a robust platform for surface-enhanced Raman spectroscopy. **2018,** *140* (4), 1247-1250.
65. Hopkinson, M. N.; Richter, C.; Schedler, M.; Glorius, F., An overview of N-heterocyclic carbenes. *Nature* **2014,** *510* (7506), 485-496.
66. Crudden, C. M.; Horton, J. H.; Narouz, M. R.; Li, Z.; Smith, C. A.; Munro, K.; Baddeley, C. J.; Larrea, C. R.; Drevniok, B.; Thanabalasingam, B., Simple direct formation of self-assembled N-heterocyclic carbene monolayers on gold and their application in biosensing. **2016,** *7* (1), 1-7.
67. Bora, T. J.; Precious Metals-Properties, N. E.; Applications, Recent developments on metal nanoparticles for SERS applications. **2018,** *6*, 117-13.
68. Zeman, E. J.; Schatz, G. C., An accurate electromagnetic theory study of surface enhancement factors for silver, gold, copper, lithium, sodium, aluminum, gallium, indium, zinc, and cadmium. **1987,** *91* (3), 634-643.
69. Pemberton, J. E.; Girand, M. M., Electrochemical and sem characterization of Ag electrodes roughened by potential sweep and potential step processes in aqueous chloride and chloride + pyridine media. *Journal of Electroanalytical Chemistry and Interfacial Electrochemistry* **1987,** *217* (1), 79-92.
70. Brolo, A. G.; Irish, D. E.; Smith, B. D., Applications of surface enhanced Raman scattering to the study of metal-adsorbate interactions. *Journal of Molecular Structure* **1997,** *405* (1), 29-44.
71. Tuschel, D. D.; Pemberton, J. E.; Cook, J. E., SERS and SEM of roughened silver electrode surfaces formed by controlled oxidation-reduction in aqueous chloride media. *Langmuir* **1986,** *2* (4), 380-388.
72. Tahghighi, M.; Janner, D.; Ignés-Mullol, J., Optimizing Gold Nanoparticle Size and Shape for the Fabrication of SERS Substrates by Means of the Langmuir–Blodgett Technique. *Nanomaterials (Basel, Switzerland)* **2020,** *10* (11), 2264.
73. Zhong, M.; Brolo, A. G. Evaluation of substrates for surface-enhanced Raman scattering. [University of Victoria], Victoria, British Columbia, 2016.
74. Frisch, M. J.; Trucks, G. W.; Schlegel, H. B.; Scuseria, G. E.; Robb, M. A.; Cheeseman, J. R.; Scalmani, G.; Barone, V.; Petersson, G. A.; Nakatsuji, H.; Li, X.; Caricato, M.; Marenich, A. V.; Bloino, J.; Janesko, B. G.; Gomperts, R.; Mennucci, B.; Hratchian, H. P.; Ortiz, J. V.; Izmaylov, A. F.; Sonnenberg, J. L.; Williams; Ding, F.; Lipparini, F.; Egidi, F.; Goings, J.; Peng, B.; Petrone, A.; Henderson, T.; Ranasinghe, D.; Zakrzewski, V. G.; Gao, J.; Rega, N.; Zheng, G.; Liang, W.; Hada, M.; Ehara, M.; Toyota, K.; Fukuda, R.; Hasegawa, J.; Ishida, M.; Nakajima, T.; Honda, Y.; Kitao, O.; Nakai, H.; Vreven, T.; Throssell, K.; Montgomery Jr., J. A.; Peralta, J. E.; Ogliaro, F.; Bearpark, M. J.; Heyd, J. J.; Brothers, E. N.; Kudin, K. N.; Staroverov, V. N.; Keith, T. A.; Kobayashi, R.; Normand, J.; Raghavachari, K.; Rendell, A. P.; Burant, J. C.; Iyengar,

S. S.; Tomasi, J.; Cossi, M.; Millam, J. M.; Klene, M.; Adamo, C.; Cammi, R.; Ochterski, J. W.; Martin, R. L.; Morokuma, K.; Farkas, O.; Foresman, J. B.; Fox, D. J. *Gaussian 16 Rev. C.01*, Wallingford, CT, 2016.
75. Dennington, R.; Keith, T.; Millam, J., Shawnee Mission, KS, GaussView, Version 4.1. 2. **2007**.
76. Trujillo, M. J.; Strausser, S. L.; Becca, J. C.; DeJesus, J. F.; Jensen, L.; Jenkins, D. M.; Camden, J. P., Using SERS To Understand the Binding of N-Heterocyclic Carbenes to Gold Surfaces. *The Journal of Physical Chemistry Letters* **2018,** *9* (23), 6779-6785.
77. DeJesus, J. F.; Trujillo, M. J.; Camden, J. P.; Jenkins, D. M., N-Heterocyclic Carbenes as a Robust Platform for Surface-Enhanced Raman Spectroscopy. *Journal of the American Chemical Society* **2018,** *140* (4), 1247-1250.
78. Socrates, G., Infrared and Raman characteristic group frequencies: tables and charts. John Wiley & Sons: 2004.
79. Zou, S.; Williams, C. T.; Chen, E. K. Y.; Weaver, M. J., Surface-Enhanced Raman Scattering as a Ubiquitous Vibrational Probe of Transition-Metal Interfaces: Benzene and Related Chemisorbates on Palladium and Rhodium in Aqueous Solution. *The Journal of Physical Chemistry B* **1998,** *102* (45), 9039-9049.
80. Zhukhovitskiy, A. V.; Mavros, M. G.; Van Voorhis, T.; Johnson, J. A., Addressable carbene anchors for gold surfaces. **2013,** *135* (20), 7418-7421.
81. Wang, G.; Rühling, A.; Amirjalayer, S.; Knor, M.; Ernst, J. B.; Richter, C.; Gao, H.-J.; Timmer, A.; Gao, H.-Y.; Doltsinis, N. L., Ballbot-type motion of N-heterocyclic carbenes on gold surfaces. **2017,** *9* (2), 152-156.
82. Lin, Y.; Firdaus, Y.; Isikgor, F. H.; Nugraha, M. I.; Yengel, E.; Harrison, G. T.; Hallani, R.; El-Labban, A.; Faber, H.; Ma, C., Self-assembled monolayer enables hole transport layer-free organic solar cells with 18% efficiency and improved operational stability. **2020,** *5* (9), 2935-2944.
83. Malham, I. B.; Bureau, L. J., Growth and stability of a self-assembled monolayer on plasma-treated mica. **2009,** *25* (10), 5631-5636.
84. Flynn, N. T.; Tran, T. N. T.; Cima, M. J.; Langer, R. J., Long-term stability of self-assembled monolayers in biological media. **2003,** *19* (26), 10909-10915.
85. Veinot, A. J.; Al-Rashed, A.; Padmos, J. D.; Singh, I.; Lee, D. S.; Narouz, M. R.; Lummis, P. A.; Baddeley, C. J.; Crudden, C. M.; Horton, J. H. J. C. A. E. J., N-Heterocyclic Carbenes Reduce and Functionalize Copper Oxide Surfaces in One Pot. **2020,** *26* (50), 11431-11434.
86. Jiang, L.; Zhang, B.; Médard, G.; Seitsonen, A. P.; Haag, F.; Allegretti, F.; Reichert, J.; Kuster, B.; Barth, J. V.; Papageorgiou, A. C., N-Heterocyclic carbenes on close-packed coinage metal surfaces: bis-carbene metal adatom bonding scheme of monolayer films on Au, Ag and Cu. **2017,** *8* (12), 8301-8308.
87. Newman, C. P.; Clarkson, G. J.; Rourke, J. P., Silver(I) N-heterocyclic carbene halide complexes: A new bonding motif. *Journal of Organometallic Chemistry* **2007,** *692* (22), 4962-4968.
88. Citadelle, C. A.; Nouy, E. L.; Bisaro, F.; Slawin, A. M. Z.; Cazin, C. S., Simple and versatile synthesis of copper and silver N-heterocyclic carbene complexes in water or organic solvents. *Dalton Transactions* **2010,** *39* (19), 4489-4491.
89. Nakano, Y.; Sakaguchi, S., Inversions in asymmetric conjugate addition reaction of cyclic enones catalyzed by the Cu/NHC-AgX system: Factors affecting the stereoselective

formation of both enantiomers. *Journal of Organometallic Chemistry* **2017,** *846*, 407-416.
90. Dible, B. R.; Sigman, M. S.; Arif, A. M., Oxygen-Induced Ligand Dehydrogenation of a Planar Bis-μ-Chloronickel(I) Dimer Featuring an NHC Ligand. *Inorganic Chemistry* **2005,** *44* (11), 3774-3776.
91. Youn, S. W.; Yoo, H. J., One-Pot Sequential N-Heterocyclic Carbene/Rhodium(III) Catalysis: Synthesis of Fused Polycyclic Isocoumarins. **2017,** *359* (13), 2176-2183.
92. Savoie, J.; Stenne, B.; Collins, S. K., Improved Chiral Olefin Metathesis Catalysts: Increasing the Thermal and Solution Stability via Modification of a C1-Symmetrical N-Heterocyclic Carbene Ligand. **2009,** *351* (11-12), 1826-1832.
93. Ikhile, M. I.; Bala, M. D., Structures of N,N'-bis(tert-Butyl)-N-Formylethylenediamine Halides obtained by Salt Metathesis from Metal Precursors. *Journal of Chemical Crystallography* **2013,** *43* (2), 76-81.
94. Kolychev, E. L.; Shuntikov, V. V.; Khrustalev, V. N.; Bush, A. A.; Nechaev, M. S., Dual reactivity of N-heterocyclic carbenes towards copper(ii) salts. *Dalton Transactions* **2011,** *40* (12), 3074-3076.
95. Astakhov, A. V.; Khazipov, O. V.; Chernenko, A. Y.; Pasyukov, D. V.; Kashin, A. S.; Gordeev, E. G.; Khrustalev, V. N.; Chernyshev, V. M.; Ananikov, V. P., A New Mode of Operation of Pd-NHC Systems Studied in a Catalytic Mizoroki–Heck Reaction. *Organometallics* **2017,** *36* (10), 1981-1992.
96. Khazipov, O. V.; Shevchenko, M. A.; Chernenko, A. Y.; Astakhov, A. V.; Pasyukov, D. V.; Eremin, D. B.; Zubavichus, Y. V.; Khrustalev, V. N.; Chernyshev, V. M.; Ananikov, V. P., Fast and Slow Release of Catalytically Active Species in Metal/NHC Systems Induced by Aliphatic Amines. *Organometallics* **2018,** *37* (9), 1483-1492.
97. Gordeev, E. G.; Eremin, D. B.; Chernyshev, V. M.; Ananikov, V. P., Influence of R–NHC Coupling on the Outcome of R–X Oxidative Addition to Pd/NHC Complexes (R = Me, Ph, Vinyl, Ethynyl). *Organometallics* **2018,** *37* (5), 787-796.
98. Williams, T. J.; Bray, J. T. W.; Lake, B. R. M.; Willans, C. E.; Rajabi, N. A.; Ariafard, A.; Manzini, C.; Bellina, F.; Whitwood, A. C.; Fairlamb, I. J., Mechanistic Elucidation of the Arylation of Non-Spectator N-Heterocyclic Carbenes at Copper Using a Combined Experimental and Computational Approach. *Organometallics* **2015,** *34* (14), 3497-3507.
99. Li, D.; Ollevier, T. J., Mechanism studies of oxidation and hydrolysis of Cu(II NHC and Ag NHC in solution under air. **2020,** *906*, 121025.
100. Lombardi, J. R.; Birke, R. L., A unified approach to surface-enhanced Raman spectroscopy. **2008,** *112* (14), 5605-5617.
101. Brolo, A. G.; Germain, P.; Hager, G. J., Investigation of the adsorption of L-cysteine on a polycrystalline silver electrode by surface-enhanced Raman scattering (SERS) and surface-enhanced second harmonic generation (SESHG). **2002,** *106* (23), 5982-5987.
102. Brolo, A. G.; Irish, D. E, The adsorption and orientation of pyrazine on silver electrodes: a surface enhanced Raman scattering study. **1996,** *414* (2), 183-196.
103. Brolo, A.; Temperini, M.; Agostinho, S. J., Copper dissolution in bromide medium in the absence and presence of hexamethylenetetramine (HMTA). **1998,** *44* (4), 559-571.
104. Corn, R. M.; Higgins, D. A., Optical second harmonic generation as a probe of surface chemistry. **1994,** *94* (1), 107-125.
105. Larkin, D.; Guyer, K. L.; Hupp, J. T.; Weaver, M. J.; Electrochemistry, I., Determination of specific adsorption of some simple anions at a polycrystalline silver-

aqueous interface using differential capacitance and kinetic probe techniques. **1982,** *138* (2), 401-423.
106. Brolo, A. G., Plasmonics for future biosensors. **2012,** *6* (11), 709-713.
107. Mayer, K. M.; Hafner, J. H., Localized surface plasmon resonance sensors. **2011,** *111* (6), 3828-3857.
108. Gao, X.; Davies, J. P.; Weaver, M. J., Test of surface selection rules for surface-enhanced Raman scattering: the orientation of adsorbed benzene and monosubstituted benzenes on gold. **1990,** *94* (17), 6858-6864.
109. Zou, S.; Williams, C. T.; Chen, E. K.-Y.; Weaver, M. J., Surface-enhanced Raman scattering as a ubiquitous vibrational probe of transition-metal interfaces: benzene and related chemisorbates on palladium and rhodium in aqueous solution. **1998,** *102* (45), 9039-9049.